Research Square

Preprints are preliminary reports that have not undergone peer review.
They should not be considered conclusive, used to inform clinical practice,
or referenced by the media as validated information.

A unified rate-dependent anisotropic hysteresis model for grain-oriented, non-oriented, and directional electrical steels

Mario Bendra

Mario.Bendra@jku.at

Johannes Kepler University of Linz

Florian Poltschak

Johannes Kepler University of Linz

Article

Keywords:

Posted Date: August 7th, 2026

DOI: https://doi.org/10.21203/rs.3.rs-10537446/v1

License: This work is licensed under a Creative Commons Attribution 4.0 International License.
Read Full License

Additional Declarations: No competing interests reported.

A unified rate-dependent anisotropic hysteresis model for grain-oriented, non-oriented, and directional electrical steels

Mario Bendra [1,*] **and Florian Poltschak** [1]

[1]JKU Hoerbiger Research Institute for Smart Actuators, Altenberger Strasse 69, Science Park 1, 4040 Linz, Austria
[*]mario.bendra@jku.at

ABSTRACT

Commercial finite-element packages handle grain-oriented electrical steels through scalar Jiles–Atherton or Preisach laws that require per-direction refitting and cannot predict cross-direction loop shapes from a single parameter set. The published Jiles-anisotropic fit to Hi-B 27M-OH absorbs this gap in a nonphysical $35\,\%$ direction dependence of the saturation magnetization. Here we present a vector Fokker–Planck model on the orientation sphere S^2 that couples Zeeman, uniaxial, and cubic anisotropies into a single free-energy landscape, solved with a Chang–Cooper well-balanced flux scheme that makes the Boltzmann distribution the exact discrete kernel. A shared base $(M_\mathrm{s}, a, \alpha, K_\mathrm{u}, D)$ with frequency-dependent $K_1(f)$ and $\tau_\mathrm{R}(f)$ fits rolling- and transverse-direction Hi-B 27M-OH loops at 50 to $200\,\mathrm{Hz}$ to mean $\mathrm{RMSE_B} = 0.069\,\mathrm{T}$, a $2\times$ transverse direction (TD) improvement over six baselines refitted per loop. The fitted corner $f_\mathrm{c} \approx 99\,\mathrm{Hz}$ coincides with the linear skin-depth crossover at the high-grain-oriented (HGO) operating-knee permeability. A texture-collapse identity reconciles the fitted $K_1 \approx 1\,\mathrm{kJ\cdot m^{-3}}$ with the single-crystal Fe-3%Si value $35\,\mathrm{kJ\cdot m^{-3}}$ via Bingham orientation distribution function (ODF) averaging, and the model reduces cleanly to the isotropic limit on non-grain-oriented (NGO) rings. The model class reproduces the Li & Luo B30P105 amplitude sweep with one Langevin scale per amplitude, while strict single-parameter-set transfer across amplitude remains an open limitation. The fitted $M_\mathrm{s} = 1.41 \times 10^6\,\mathrm{A\cdot m^{-1}}$ sits $17\,\%$ below the Fe-3%Si nominal range, a scalar-projection limitation resolved by the per-grain Landau–Lifshitz–Gilbert (LLG) infrastructure (`hysterpy.llg_grain`) validated against the Stoner–Wohlfarth astroid. All data, parameters, and the open-source `hysterpy` implementation are released as a Zenodo-archived companion.

Introduction

The orientational dynamics of an ensemble of vector quantities driven by an external field and subjected to thermal noise is the common mathematical structure underlying magnetic hysteresis in ferromagnets, dielectric relaxation in polar fluids, polymer-chain orientation under flow, and single-molecule rotational diffusion in biophysical assays[1–3]. In each case, the state is a probability density ρ on the rotation manifold (the unit circle S^1 or the unit sphere S^2). Its time evolution is governed by a Fokker–Planck equation with a drift derived from a free-energy landscape and a rotational diffusion that encodes thermal fluctuations. The mathematical universality is well established. What is less developed is a portable, validated implementation of that framework as a constitutive law for engineering-scale electromagnetic devices.

For soft electrical steels, the magnetic core material in motors, transformers, sensors, and actuators, the constitutive bottleneck is that no single hysteresis model has been shown to reproduce the qualitatively different responses of grain-oriented (GO) and NGO sheets with one physical parameter set. GO sheets such as Hi-B 27M-OH show narrow-waist, sharply-switching loops along the rolling direction (RD) and significantly broader, rate-sensitive loops along the TD[4]. NGO sheets show nearly-isotropic behavior with intrinsic body-centered-cubic anisotropy. Both families exhibit amplitude- and frequency-dependent loops that classical Jiles–Atherton (J–A)[5] captures only after per-condition refitting. State-of-the-art Jiles-family fits to RD, and TD loops on the same physical sheet require distinct M_s values that differ by $35\,\%$, an artifact of conflating the anisotropic anhysteretic shape with the hysteretic transport layer[4,6].

We address this conflation by lifting the Fokker–Planck (FP) formulation to the orientation sphere. The state variable is the full moment-orientation density $\rho(\hat{\mathbf{m}}, t)$ on S^2 rather than the in-plane projection on S^1 used in earlier scalar Jiles-family hysteresis models. The drift derives from a complete energy $U = -\mu_0 M_\mathrm{s} \mathbf{H}\cdot\hat{\mathbf{m}} - K_\mathrm{u}(\hat{\mathbf{m}}\cdot\hat{\mathbf{e}}_\mathrm{u})^2 + K_1(m_x^2 m_y^2 + m_y^2 m_z^2 + m_z^2 m_x^2)$ that contains the Zeeman, uniaxial, and BCC cubic anisotropy contributions on equal footing in the lab frame. Texture (e.g. the Goss $\{110\}\langle 001\rangle$ structure of HGO steels, in which the $\{110\}$ rolling plane is parallel to the sheet and the $\langle 001\rangle$ easy axis is parallel to the RD) enters geometrically through the orientation of $\hat{\mathbf{e}}_\mathrm{u}$ relative to the applied field. Only the lab-frame projection of the applied field changes between RD and TD measurements. For Goss-textured steels, the lab TD lies in the rolling plane $\{110\}$ perpendicular to RD, which in the cubic crystal frame is a $\langle 110\rangle$-type direction perpendicular to the $\langle 001\rangle$ easy axis.

Mean-field coupling αM along the field, an effective relaxation time τ_R in the drift, and an angular diffusion coefficient D in the noise together produce the rate-dependent loop widening characteristic of finite excitation frequency.

A challenge specific to vector Fokker–Planck on S^2 is that the straightforward latitude–longitude finite-volume discretization suffers a polar coordinate singularity that, combined with naïve explicit time integration, produces probability accumulation at the poles and a systematic bias against the Boltzmann equilibrium. We avoid this pathology by adopting the Chang–Cooper well-balanced flux discretization[7,8], in which the geometric-mean face value $\rho_{\mathrm{eq}}^{F} = (\rho_{\mathrm{eq}}^{+}\rho_{\mathrm{eq}}^{-})^{1/2}$ guarantees that the Boltzmann distribution is the exact kernel of the discrete Fokker–Planck operator. We verify this property to machine precision and combine the discretization with a Crank–Nicolson time step that is unconditionally stable and preserves the discrete equilibrium under arbitrary time steps.

This work is built around a joint fit of rolling- and transverse-direction loops of the Baghel et al. Hi-B 27M-OH (a Goss-textured HGO steel) at four frequencies 50 to 200 Hz with a *shared physical base* (M_s, a, α, K_u, D), a three-parameter phenomenological frequency-dependent cubic anisotropy $K_1(f)$, and a per-frequency relaxation time $\tau_R(f)$. The previous direction-resolved fit by Baghel et al. 2015[4] required different $(M_s, a, k, K_{1,\mathrm{eff}})$ per direction. We share all of these between RD and TD. Only the lab-frame field projection differs. Crucially, M_s is the same scalar property of the alloy in both directions, removing the nonphysical 35 % direction-dependent saturation magnetization reported by the published Jiles-anisotropic fit. Cross-model benchmarking against J–A, Chwastek modified J–A[9], the D'Aloia–Di Francesco–De Santis (DDD) elastic-collision dynamic model[10], the simplified diffusion-driven thermodynamic hysteresis model (DTHM–S) S^1 Boltzmann-Ansatz reduction of the present formulation, the Preisach operator model[11], and the Prandtl–Ishlinskii (PI) operator model[12] confirms that no published baseline matches the cross-direction unification claim with a single shared parameter set. Additional tests on the Li–Luo 2024 B30P105 HGO steel over twenty amplitude levels at 50 Hz[13] and on seven non-oriented ring-core steels (X10CrAlSi7, X20Cr13, S235JR, HLB8, HC260LA, isovac HP1400-100A, C35) covering the range of soft-magnetic alloys used in industrial electromagnetic devices demonstrate that the model reduces cleanly to the isotropic limit when the texture is absent, without spurious anisotropy.

The implementation, all measurement data, and all fitted parameter sets are released as the open-source `hysterpy` Python package, enabling the constitutive layer to be reused as a foundation for downstream electromagnetic simulations across the full range of soft-magnetic alloys.

Theory

State variable and observable

The orientation density $\rho(\hat{\mathbf{m}}, t)$, with $\hat{\mathbf{m}}$ the unit vector along the local magnetic-moment direction, is defined on the unit sphere S^2 for the vectorial formulation, or on its in-plane reduction $\rho(\theta, t)$ on the unit circle S^1. In either case

$$\int \rho \, \mathrm{d}\Omega \;=\; 1, \qquad \rho \geq 0, \tag{1}$$

where $\mathrm{d}\Omega$ denotes the integration measure of the orientation manifold (the solid-angle element $\sin\theta \, \mathrm{d}\theta \, \mathrm{d}\phi$ on S^2, the arc element $\mathrm{d}\theta$ on S^1), and the macroscopic magnetization along an arbitrary lab-frame unit direction $\hat{\mathbf{u}}$ is the corresponding moment of ρ,

$$M_{\hat{\mathbf{u}}}(t) \;=\; M_s \int (\hat{\mathbf{m}} \cdot \hat{\mathbf{u}}) \, \rho(\hat{\mathbf{m}}, t) \, \mathrm{d}\Omega. \tag{2}$$

The flux density follows from the standard linear constitutive relation

$$\mathbf{B}(t) \;=\; \mu_0 \big(\mathbf{H}(t) + \mathbf{M}(t) \big). \tag{3}$$

For the in-plane reduction, the macroscopic magnetization is the first cosine moment,

$$M(t) \;=\; M_s \int_{-\pi}^{\pi} \cos\theta \, \rho(\theta, t) \, \mathrm{d}\theta. \tag{4}$$

Three observable scalar quantities characterize each measured loop and serve as gauge quantities reported alongside RMSE_B: the coercive field H_c, defined implicitly as the field at which the induction crosses zero on a given branch, the remanent flux density B_r, defined as the induction remaining when the field returns to zero, and the hysteretic loop area A_{loop} (which equals the per-cycle energy dissipated per unit volume),

$$B(H = H_c) = 0, \qquad B_r = B(H = 0), \qquad A_{\mathrm{loop}} = \oint H \, \mathrm{d}B. \tag{5}$$

Vector Fokker–Planck evolution

Out of equilibrium, the orientation density evolves under the Fokker–Planck equation[1,2],

$$\frac{\partial \rho}{\partial t} \;=\; -\nabla_S \cdot \big[\, \mathbf{v}\, \rho \,\big] \;+\; D \nabla_S^2 \rho, \tag{6}$$

with ∇_S and ∇_S^2 the surface gradient and Laplace–Beltrami operator on the orientation manifold. The bracketed product $\mathbf{v}\,\rho$ is the advective probability flux (drift velocity times density), so the first term transports probability along the drift while the second term spreads it diffusively. The diffusion coefficient D obeys the Einstein fluctuation–dissipation relation

$$D \;=\; \frac{k_\mathrm{B} T}{\mu_0 M_\mathrm{s} a\, \tau_\mathrm{R}}, \tag{7}$$

where τ_R is the rotational relaxation time, and the thermal-energy scale is

$$a \;=\; \frac{k_\mathrm{B} T}{\mu_0 M_\mathrm{s}\, v_0} \tag{8}$$

with v_0 the volume of the elementary single-domain particle. Combining equations (7) and (8) gives the canonical fluctuation–dissipation product

$$D\, \tau_\mathrm{R}\, \mu_0 M_\mathrm{s} a \;=\; k_\mathrm{B} T, \tag{9}$$

which guarantees the Boltzmann distribution at temperature T as the unique stationary solution of equation (6). In this work, D is fitted as a free parameter rather than computed from T, which absorbs per-sample variations in the elementary volume of coherent rotation v_0.

The drift velocity decomposes into Zeeman, uniaxial-anisotropy, and cubic-anisotropy contributions,

$$\mathbf{v} \;=\; \mathbf{v}_\mathrm{Zeeman} + \mathbf{v}_{K_\mathrm{u}} + \mathbf{v}_{K_1}, \tag{10}$$

each derived from the corresponding term in the free energy $U(\hat{\mathbf{m}})$ via $\mathbf{v} = -\nabla_S U/(\mu_0 M_\mathrm{s} a \tau_\mathrm{R})$. For the in-plane S^1 reduction with angle θ measured from the field direction, and introducing the Weiss effective field $H_\mathrm{e} = H + \alpha M$ with mean-field coupling α,

$$v_\mathrm{Zeeman}(\theta) = -\,\frac{1}{\tau_\mathrm{R}}\, \sin\theta\, \frac{H_\mathrm{e}}{a}, \tag{11}$$

$$v_{K_\mathrm{u}}(\theta) = -\,\frac{K_\mathrm{u}}{\mu_0 M_\mathrm{s}\, a\, \tau_\mathrm{R}}\, \sin\!\big(2(\theta - \phi_\mathrm{easy})\big), \tag{12}$$

$$v_{K_1}(\theta) = -\,\frac{K_1}{\mu_0 M_\mathrm{s}\, a\, \tau_\mathrm{R}}\, \sin(4\theta), \tag{13}$$

where ϕ_easy is the per-sample uniaxial easy-axis rotation relative to the lab frame and the cubic term is lab-aligned (consistent with the Ramesh–Jiles–Bi 1997 convention[14]). The Weiss effective field is defined explicitly as

$$H_\mathrm{e}(t) \;=\; H(t) + \alpha\, M(t), \tag{14}$$

For Goss-textured polycrystals, the mean-field coupling is anisotropic in the lab frame: the inter-grain exchange seen by spins inside a crystal whose [001] axis lies parallel to the applied field (parallel cuts) differs from that seen by spins in grains whose [001] axis is perpendicular to the applied field, because the spin-wave dispersion sampled along the two directions probes different sub-spaces of the cubic lattice[15,16]. We retain this asymmetry by replacing the scalar α with two coefficients, $\alpha_\parallel$ along the crystal [001] easy axis and $\alpha_\perp$ in the perpendicular plane, projected onto each grain's local field axis as $\alpha_\mathrm{eff}(\hat{\mathbf{n}}_\mathrm{f}) = \alpha_\parallel\, (\hat{\mathbf{n}}_\mathrm{f} \cdot \hat{\mathbf{e}}_\mathrm{u})^2 + \alpha_\perp\, [1 - (\hat{\mathbf{n}}_\mathrm{f} \cdot \hat{\mathbf{e}}_\mathrm{u})^2]$. The isotropic limit $\alpha_\parallel = \alpha_\perp$ recovers the single-scalar formulation used by Jiles and Atherton[5]. And the drift (10) can be written equivalently in micromagnetic form as the projection of the total effective field on the unit tangent $\hat{\theta}$ to the orientation circle,

$$v(\theta) \;=\; -\,\frac{1}{\tau_\mathrm{R}\, a}\, \big[H_\mathrm{e}\, \hat{\mathbf{z}} + \mathbf{H}_\mathrm{ani}^\mathrm{uni} + \mathbf{H}_\mathrm{ani}^\mathrm{cub}\big] \cdot \hat{\theta}, \tag{15}$$

with the anisotropy effective fields defined below in equations (19) and (23). The four physical processes, Zeeman driving, uniaxial texture, cubic crystallography, and thermal diffusion, enter through symmetry-distinct terms ($\sin\theta$, $\sin 2(\theta - \phi_\mathrm{easy})$, $\sin 4\theta$, second-order spatial derivative, respectively), which is what enables their joint identification from multi-condition data.

Free-energy landscape

For the vectorial S^2 formulation, the total free energy combines Zeeman, uniaxial, and cubic anisotropy contributions on equal footing in the lab frame:

$$U(\hat{\mathbf{m}}) = -\mu_0 M_\mathrm{s}\,\mathbf{H}\cdot\hat{\mathbf{m}} - K_\mathrm{u}(\hat{\mathbf{m}}\cdot\hat{\mathbf{e}}_\mathrm{u})^2 + K_1\big(m_x^2 m_y^2 + m_y^2 m_z^2 + m_z^2 m_x^2\big), \tag{16}$$

with the uniaxial easy axis $\hat{\mathbf{e}}_\mathrm{u}$, a unit vector in the lab frame, and the cubic axes aligned with the lab basis $\hat{\mathbf{x}},\hat{\mathbf{y}},\hat{\mathbf{z}}$. Texture relative to the cubic crystal, the Goss orientation in HGO sheets, $\hat{\mathbf{e}}_\mathrm{u} \parallel \langle 100\rangle$ in the rolling direction, enters geometrically: the only thing that changes between rolling- and transverse-direction measurements on the same sheet is the lab-frame projection $\hat{\mathbf{u}}$ of the applied field. This is the structural basis of the cross-direction unification claim demonstrated in Results.

The crystal-anisotropy energy densities in equation (16) have the standard micromagnetic form[15,17]. For a single uniaxial easy axis along the unit vector $\hat{\mathbf{e}}$, the energy density admits an even expansion in the projection $\hat{\mathbf{m}}\cdot\hat{\mathbf{e}}$ of the moment direction onto the easy axis,

$$\mathscr{E}_\mathrm{ani}^\mathrm{uni} = \int_\Omega \big[K_\mathrm{u1}(\hat{\mathbf{m}}\cdot\hat{\mathbf{e}})^2 + K_\mathrm{u2}(\hat{\mathbf{m}}\cdot\hat{\mathbf{e}})^4 + \mathscr{O}((\hat{\mathbf{m}}\cdot\hat{\mathbf{e}})^6)\big]\,\mathrm{d}\mathbf{x}, \tag{17}$$

with Ω the sample volume (not to be confused with the orientation-space measure $\mathrm{d}\Omega$ of equation (1)), which we truncate to the lowest order with the sign convention[18]

$$\mathscr{E}_\mathrm{ani}^\mathrm{uni} = -\int_\Omega K_\mathrm{u}\,(\hat{\mathbf{m}}\cdot\hat{\mathbf{e}})^2\,\mathrm{d}\mathbf{x}. \tag{18}$$

For $K_\mathrm{u} > 0$ the minima lie along $\pm\hat{\mathbf{e}}$. $K_\mathrm{u} < 0$ recovers easy-plane anisotropy. The corresponding effective field is

$$\mathbf{H}_\mathrm{ani}^\mathrm{uni} \;=\; \frac{2K_\mathrm{u}}{\mu_0 M_\mathrm{s}}\,(\hat{\mathbf{m}}\cdot\hat{\mathbf{e}})\,\hat{\mathbf{e}}. \tag{19}$$

Easy-plane (planar) anisotropy corresponds to $K_\mathrm{u} < 0$. To avoid carrying a negative coefficient, we define $K_\mathrm{p} \equiv -K_\mathrm{u}$, which is positive in this regime, and write

$$\mathscr{E}_\mathrm{ani}^\mathrm{planar} = \int_\Omega K_\mathrm{p}\,(\hat{\mathbf{m}}\cdot\hat{\mathbf{e}})^2\,\mathrm{d}\mathbf{x}, \tag{20}$$

with an effective field

$$\mathbf{H}_\mathrm{ani}^\mathrm{planar} \;=\; -\frac{2K_\mathrm{p}}{\mu_0 M_\mathrm{s}}\,(\hat{\mathbf{m}}\cdot\hat{\mathbf{e}})\,\hat{\mathbf{e}}, \tag{21}$$

representing the regime in which the magnetization prefers the plane orthogonal to $\hat{\mathbf{e}}$ (ultrathin films, surface-pinned layers). This regime is not encountered in our bulk-electrical-steel validation set and is shown in Figure 1(b,e) only for completeness.

For cubic-lattice materials (bcc iron, fcc nickel), the energy density depends on projections of $\hat{\mathbf{m}}$ onto three orthogonal crystal axes $\hat{\mathbf{e}}_1,\hat{\mathbf{e}}_2,\hat{\mathbf{e}}_3$ with $\hat{\mathbf{e}}_i\cdot\hat{\mathbf{e}}_j = \delta_{ij}$. Writing $m_i = \hat{\mathbf{m}}\cdot\hat{\mathbf{e}}_i$,

$$\mathscr{E}_\mathrm{ani}^\mathrm{cub} = \int_\Omega \big[K_\mathrm{c1}(m_1^2 m_2^2 + m_2^2 m_3^2 + m_3^2 m_1^2) + K_\mathrm{c2}\,m_1^2 m_2^2 m_3^2\big]\,\mathrm{d}\mathbf{x}. \tag{22}$$

The corresponding effective field is

$$\mathbf{H}_\mathrm{ani}^\mathrm{cub} \;=\; -\frac{2}{\mu_0 M_\mathrm{s}}\,\mathsf{D}\,\hat{\mathbf{m}}, \tag{23}$$

with D the diagonal matrix whose entries depend on the m_i^2 in the standard way[17]. For bulk bcc iron, $K_\mathrm{c1} > 0$, and the $\langle 100\rangle$ directions are easy. The second-order term K_c2 is typically one order of magnitude smaller than K_c1[15] and is neglected ($K_\mathrm{c2} = 0$) in all fits reported here. However, the simulator implementation accepts non-zero K_c2 for future extensions to materials in which the higher-order cubic invariant matters. The constants in equations (12)–(13) are identified as

$$K_\mathrm{u} \equiv K_\mathrm{u1} \quad \text{(uniaxial, first order)}, \tag{24}$$

$$K_1 \equiv K_\mathrm{c1} \quad \text{(cubic, first order)}. \tag{25}$$

Equation (15) is then equivalent to $v(\theta) = -(\partial_\theta U)/(\mu_0 M_s a\,\tau_R)$ with $U(\theta)$ the in-plane reduction of equation (16). The in-plane projection of the cubic invariant follows from substituting $\hat{\mathbf{m}} = (\cos\theta, \sin\theta, 0)$ into equation (22): only the first term survives, giving

$$m_x^2 m_y^2 + m_y^2 m_z^2 + m_z^2 m_x^2 \xrightarrow{m_z=0} \cos^2\theta \sin^2\theta \;=\; \tfrac{1}{8}\big(1 - \cos 4\theta\big). \tag{26}$$

The factor-of-two discrepancy between the prefactor in equation (28) below ($\frac{1}{4}$) and the bare in-plane projection ($\frac{1}{8}$) is absorbed into the in-plane definition of K_1 used by the dynamic S^1 solver. The relation to the bulk bcc-iron cubic constant is $K_1^{S^1} = 2K_1^{S^2}$ when the same lattice physics is mapped onto the in-plane reduction.

Figure 1(**a**–**c**) visualizes the three canonical crystal-anisotropy energy surfaces underlying these terms: uniaxial, planar (included for completeness, not activated in this work), and cubic. The corresponding Boltzmann equilibrium densities on the orientation sphere S^2 from equation (27) are shown in Figure 1(**d**–**f**). Discrete 90°-wall switching events on cubic-perpendicular cuts (e.g. the transverse direction of HGO sheet) that the rotation-only Fokker–Planck operator above does not capture are handled by a separate Preisach-type hysteron overlay introduced in the Methods subsection "Domain-wall hysteron overlay". The overlay is an additive correction to the rotational dynamics, not a modification of the energy landscape in equation (16).

Boltzmann equilibrium and the anisotropic anhysteretic

At thermodynamic equilibrium in effective field H_e, equation (6) admits the Boltzmann distribution

$$\rho_{eq}(\hat{\mathbf{m}}) \;=\; Z^{-1} \exp\!\big[-U(\hat{\mathbf{m}})/(\mu_0 M_s a)\big], \tag{27}$$

with the partition function Z normalizing ρ_{eq} to unity. The in-plane reduction of the effective potential combines the Zeeman term with the truncated uniaxial energy (equation (18)) and the lab-aligned cubic energy (equation (22) restricted to the in-plane parameterization),

$$U(\theta) = -\mu_0 M_s H_e \cos\theta - K_u \cos^2(\theta - \phi_{easy}) + \tfrac{1}{4} K_1 \big(1 - \cos 4\theta\big). \tag{28}$$

With $K_u > 0$ the uniaxial term lowers U along $\theta = \phi_{easy}$ (easy-axis alignment). With $K_1 > 0$ the cubic term lowers U at $\theta \in \{0, \pi/2, \pi, 3\pi/2\}$ (cubic easy directions). Integrating equation (2) against ρ_{eq} yields the anisotropic anhysteretic explicitly,

$$M_{an}^{aniso}(H_e; K_u, K_1, \hat{\mathbf{e}}_u) \;=\; M_s \,\frac{\int_{S^2} (\hat{\mathbf{m}}\cdot\hat{\mathbf{u}}) \exp[-U(\hat{\mathbf{m}})/(\mu_0 M_s a)]\,\mathrm{d}\Omega}{\int_{S^2} \exp[-U(\hat{\mathbf{m}})/(\mu_0 M_s a)]\,\mathrm{d}\Omega}. \tag{29}$$

For $K_u = K_1 = 0$ the orientation integral is axisymmetric about the field direction and equation (29) reduces to the isotropic Langevin form

$$M_{an}(H_e) = M_s \,\mathscr{L}(H_e/a), \qquad \mathscr{L}(x) = \coth x - 1/x. \tag{30}$$

The cubic case in Figure 1(**f**) recovers the six-lobed $\langle 100 \rangle$ structure of bulk bcc iron and is the static counterpart of the dynamic vector Fokker–Planck solver verified to machine precision in Results.

Connection to the Brown–Landau–Lifshitz–Gilbert effective field

Equation (6) can be read as a coarse-graining of the micromagnetic effective field $\mathbf{H}_{eff} = -(\mu_0 M_s)^{-1}\,\delta E/\delta \mathbf{M}$ to the spatially uniform single-moment limit. Term by term, the macroscopic surrogates are: (i) the applied field $\mathbf{H}_{ext} \to \mathbf{H}$. (ii) the magnetocrystalline contribution $\mathbf{H}_{aniso} = -\nabla_S (K_u(\hat{\mathbf{m}}\cdot\hat{\mathbf{e}}_u)^2 + K_1(\cdots))/(\mu_0 M_s)$, identical to the angular gradient of the second and third terms of equation (16). (iii) the demagnetizing field $\mathbf{H}_{demag} = -\mathsf{N}\,\mathbf{M}$, with N the demagnetizing tensor, which vanishes for closed-flux samples (toroid, Epstein frame, single-sheet tester) and is otherwise absorbed into a Stoner shape correction added to $\mathbf{H}$. (iv) the exchange field $\mathbf{H}_{exch} \propto \nabla^2 \mathbf{M}$ is identically zero under the spatially uniform single-moment Ansatz used here, and is replaced by the Weiss mean-field surrogate αM entering through H_e. (v) Gilbert damping $\alpha_G\,\mathbf{M}\times\dot{\mathbf{M}}$ is encoded by the relaxation time τ_R, while Brownian thermal noise gives the diffusion term $D\nabla_S^2\rho$ in equation (6). The present model, therefore, occupies the regime in which spatial gradients are integrated out (no domain-wall structure, no exchange length), but anisotropy, Zeeman, mean-field coupling, damping, and stochastic relaxation are retained on the orientational manifold.

Reduction to established models

Two limiting cases recover J–A[5] and Jiles-anisotropic (Ramesh–Jiles–Bi 1997[14]) exactly. A third reduction, the DTHM–S S^1 Boltzmann-Ansatz formulation introduced below, is a natural simplification of the present S^2 formulation rather than a recovery

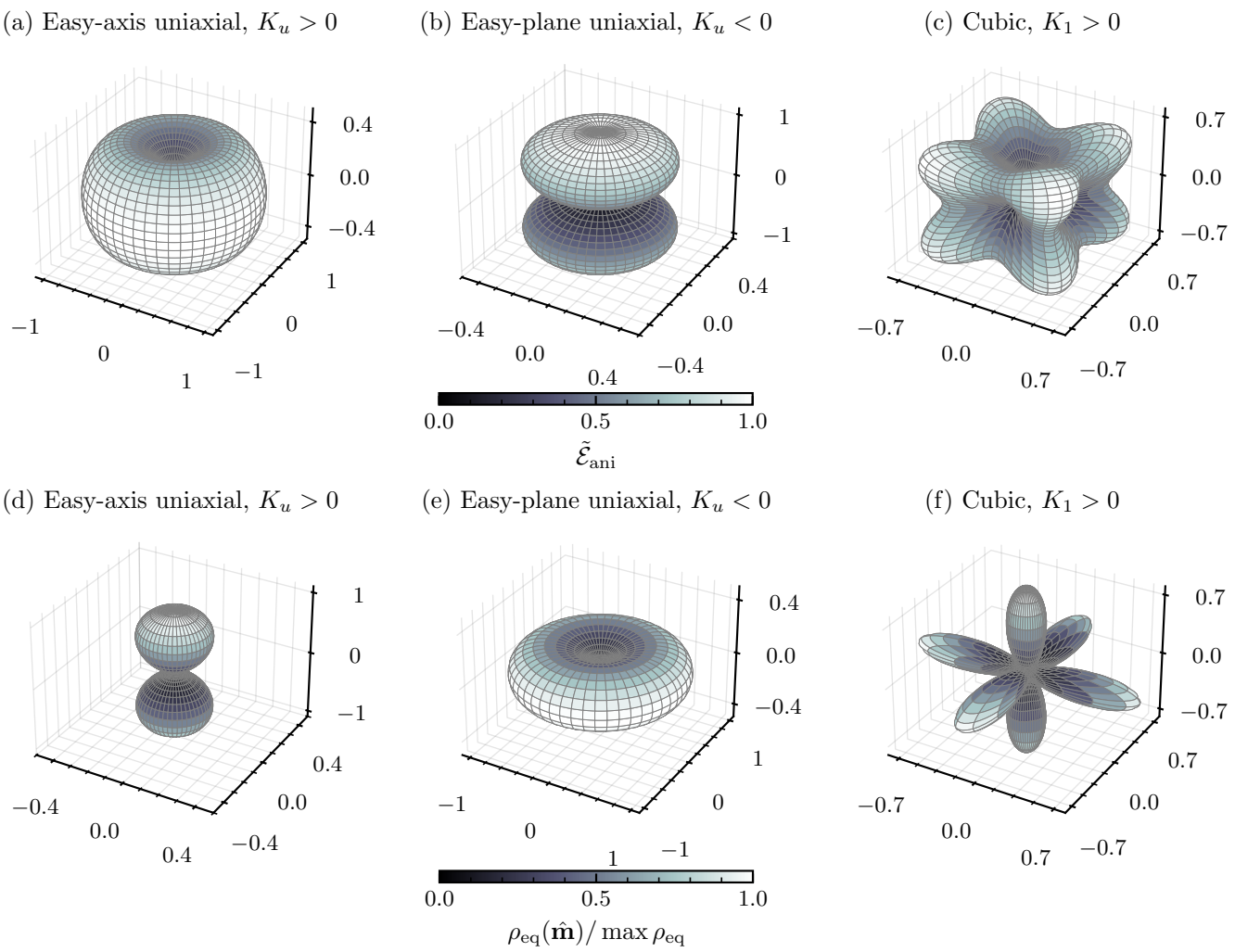

Figure 1. Free-energy landscapes (top row) and Boltzmann equilibrium densities (bottom row) for the three canonical crystal-anisotropy classes on the unit sphere of moment orientations. The top row visualizes the energy surfaces in equations (17) and (22), with the corresponding ρ_{eq} from equation (27) encoded as a radial displacement of the unit sphere in the bottom row. (**a**,**d**): Uniaxial anisotropy ($K_{\mathrm{u}} > 0$) with easy axis $\hat{\mathbf{e}}_{\mathrm{u}} = \hat{\mathbf{z}}$: two energy minima along $\pm\hat{\mathbf{e}}_{\mathrm{u}}$, two equal density lobes. Drives the Goss-texture term (12) that underlies grain-oriented electrical steels. (**b**,**e**): Planar anisotropy ($K_{\mathrm{p}} > 0$): equatorial easy plane (energy minima on the equator, density disc). Not activated in the present model. (**c**,**f**): Cubic anisotropy ($K_1 > 0$, bcc iron): six $\langle 100 \rangle$ minima and a six-lobed density, driving the lab-aligned term in equation (13). The macroscopic magnetization follows from the projection of the density onto the applied-field direction via equation (2).

of a published model. These reductions anchor the present formulation in decades of prior work and define analytic verification targets.

Isotropic J–A. Setting $K_u = K_1 = 0$ and $D \to 0$, equation (6) becomes the deterministic transport equation

$$\frac{\partial \rho}{\partial t} + \frac{\partial}{\partial \theta}[v(\theta)\,\rho] = 0, \qquad v(\theta) = -\frac{1}{\tau_R}\sin\theta\,\frac{H_e}{a}. \tag{31}$$

Multiplying by $\cos\theta$ and integrating over the circle yields a balance for the first cosine moment $\bar{c} = M/M_s$,

$$\frac{\mathrm{d}\bar{c}}{\mathrm{d}t} \;=\; \frac{H_e}{a\,\tau_R}\left\langle \sin^2\theta \right\rangle_\rho. \tag{32}$$

A linear-displacement-from-equilibrium moment closure[2], $\langle \sin^2\theta\rangle_\rho \approx \mathscr{L}'(H_e/a)\,(1-\bar{c}/\mathscr{L}(H_e/a))$, gives an intermediate ordinary differential equation (ODE)

$$\frac{\mathrm{d}M}{\mathrm{d}H} \;=\; \frac{M_{an}(H_e) - M}{k\,\delta - \alpha(M_{an}(H_e) - M)}, \tag{33}$$

with the J–A pinning constant $k = a\,\tau_R\,|\dot{H}|$ and $\delta = \mathrm{sgn}(\dot{H})$. Adding the reversible bulge $c\,\mathrm{d}M_{an}/\mathrm{d}H$ (unchanged by the closure) and defining $M_{irr} = (M - c\,M_{an})/(1-c)$ recovers the J–A ODE in its classical form

$$\frac{\mathrm{d}M}{\mathrm{d}H} \;=\; (1-c)\,\frac{M_{an} - M_{irr}}{k\,\delta - \alpha(M_{an} - M_{irr})} + c\,\frac{\mathrm{d}M_{an}}{\mathrm{d}H}, \tag{34}$$

equivalent to the pair

$$M = (1-c)\,M_{irr} + c\,M_{an}, \tag{35}$$

$$\frac{\mathrm{d}M_{irr}}{\mathrm{d}H} = \frac{M_{an} - M_{irr}}{k\,\delta - \alpha(M_{an} - M_{irr})}, \tag{36}$$

with the reversible-to-irreversible mixing fraction $c \in [0,1)$. The reduction is exact in the limits $D \to 0$ and linear displacement from ρ_{eq}. Corrections are $\mathscr{O}(D/\omega)$ for excitation frequency ω and $\mathscr{O}\big((1-\bar{c}^2)^2\big)$ from higher-moment closure.

Jiles-anisotropic. With $D \to 0$ but $K_u \neq 0$ or $K_1 \neq 0$, the same moment closure adds the anisotropy drift terms to equation (32), producing

$$\begin{aligned}\frac{\mathrm{d}\bar{c}}{\mathrm{d}t} =& \frac{H_e}{a\tau_R}\left\langle \sin^2\theta \right\rangle_\rho + \frac{K_u}{\mu_0 M_s a \tau_R}\left\langle \sin\theta\,\sin 2(\theta - \phi_{easy}) \right\rangle_\rho \\ &+ \frac{K_1}{\mu_0 M_s a \tau_R}\left\langle \sin 4\theta\,\sin\theta \right\rangle_\rho,\end{aligned} \tag{37}$$

in which the three averages are the Zeeman, uniaxial, and cubic drift contributions of equations (11)–(13) summed on the right-hand side (the second line continues the sum). After the Boltzmann closure, this reduces to equation (34) with M_{an} replaced by the anisotropic anhysteretic M_{an}^{aniso} from equation (27). This reproduces the Ramesh–Jiles–Bi 1997[14] extension of J–A to anisotropic materials exactly.

DTHM–S (S^1 Boltzmann-Ansatz reduction). Retaining $D > 0$ but enforcing a Boltzmann Ansatz on ρ (instantaneous equilibration of the orientation distribution at each H_e) collapses equation (6) to a Jiles-structure ODE that tracks M_{irr} separately. This reduction is constructed in the present work as a baseline against which the full S^2 formulation is benchmarked:

$$\begin{aligned} H_e &= H + \alpha M, \\ \frac{\mathrm{d}M_{irr}}{\mathrm{d}H} &= \frac{M_{an} - M_{irr}}{k\,\delta - \alpha(M_{an} - M_{irr})}, \\ M &= c\,M_{an} + (1-c)\,M_{irr}. \end{aligned} \tag{38}$$

The five-parameter structure is identical to J–A. The model differs only in its physical interpretation of a, k, c as moments of the assumed distribution rather than phenomenological constants.

Comparison baselines

For the cross-model comparison reported in Results, we additionally consider three operator-based and two phenomenological baselines, each fitted independently for each loop (favoring the baselines). The Chwastek modified J–A model[9] retains the J–A effective field (14) and the anhysteretic (30) together with the same irreversible ODE for M_{irr}, but replaces the c-weighted reversible bulge of equation (34) by a dynamic combination of anhysteretic and irreversible response,

$$M \;=\; (1-\beta)\, M_{\mathrm{an}}(H_{\mathrm{e}}) + \beta\, M_{\mathrm{irr}}, \tag{39}$$

with one extra parameter $\beta \in [0,1]$ governing how much of M follows the instantaneous anhysteretic. The DDD elastic-collision model[10] represents the magnetization rate, restricted to sinusoidal excitation $H(t) = H_0 \cos \omega t$, as

$$\frac{\mathrm{d}M}{\mathrm{d}t} = \gamma \sin(\omega t + \beta_{\mathrm{D}}) \exp\!\big(-\alpha_{\mathrm{D}} \cos^2(\omega t + \beta_{\mathrm{D}})\big). \tag{40}$$

The Preisach operator model[11] treats hysteresis as a weighted superposition of elementary relay operators $\hat{\gamma}_{\alpha,\beta}$ with up/down thresholds $\alpha \geq \beta$,

$$M[H](t) = \iint_{\alpha \geq \beta} \mu(\alpha,\beta)\, \hat{\gamma}_{\alpha,\beta}[H](t)\, \mathrm{d}\alpha\, \mathrm{d}\beta, \tag{41}$$

with the Preisach density $\mu(\alpha,\beta) \geq 0$ determined from measurement (typically a Gaussian or Lorentzian prior). The PI operator model[12] superposes play operators $\hat{p}_r[H]$ of threshold r,

$$M[H](t) = \sum_{i=1}^{N} w_i\, \hat{p}_{r_i}[H](t), \tag{42}$$

with weights and thresholds fitted from measurement. Like the Preisach model, PI is rate-independent and phenomenological. A common feature of all the prior baselines is that frequency dependence enters, if at all, through added dissipation terms ($\eta\, \dot{H}$- type) rather than from the underlying magnetization dynamics. The vector Fokker–Planck formulation places the rate dependence within the orientation distribution itself via equation (6), thereby enabling a single set of physical parameters to unify direction, amplitude, and frequency.

Methods

Numerical discretization: Chang–Cooper well-balanced flux scheme

A naïve lat–lon discretization of equation (6) on S^2 suffers two pathologies: (i) the polar coordinate singularity at $\theta \in \{0, \pi\}$ amplifies the diffusion stencil by $1/\sin\theta$, imposing severe explicit time-step restrictions. And (ii) the discrete divergence and discrete Laplacian, derived independently with separate discretization choices, do not in general admit the same Boltzmann distribution as their joint kernel, biasing the steady state away from the physical equilibrium. We avoid these pathologies by adopting the Chang–Cooper well-balanced flux formulation[7,8], which writes equation (6) in the equivalent flux form

$$\frac{\partial \rho}{\partial t} \;=\; D \nabla_S \cdot \big(\rho_{\mathrm{eq}}\, \nabla_S (\rho/\rho_{\mathrm{eq}})\big). \tag{43}$$

Discretizing on a staggered lat–lon grid with cell-center values at (θ_i, ϕ_j), $\theta_i = (i+1/2)\Delta\theta$, $\phi_j = j\Delta\phi$, the discrete face flux that gives Boltzmann as the exact kernel of the operator is[7]

$$J_F \;=\; D\, \rho_{\mathrm{eq}}^F\, \frac{(\rho/\rho_{\mathrm{eq}})^+ - (\rho/\rho_{\mathrm{eq}})^-}{\Delta}, \qquad \rho_{\mathrm{eq}}^F = \sqrt{\rho_{\mathrm{eq}}^+ \rho_{\mathrm{eq}}^-}, \tag{44}$$

where $\rho^{\pm}$ denote the cell-center values on either side of the face F, Δ is the center-to-center distance across the face, and the geometric-mean face value ρ_{eq}^F enforces detailed balance at the discrete level. Substituting $\rho^{\pm} \to \rho_{\mathrm{eq}}^{\pm}$ into equation (44) gives $J_F = 0$ on every face, so ρ_{eq} is identically a stationary solution of the discrete operator regardless of grid resolution. Polar face areas vanish ($\sin 0 = \sin \pi = 0$), so no flux passes through the singular axis. Cell volumes are $V_{i,j} = \sin\theta_i\, \Delta\theta\, \Delta\phi$, theta-face areas $A^{\theta}_{i+1/2,j} = \sin\theta_{i+1/2}\, \Delta\phi$, phi-face areas $A^{\phi}_{i,j+1/2} = \Delta\theta$ (constant in this lat–lon grid). Time stepping uses the Crank–Nicolson scheme,

$$\big(I - \tfrac{1}{2}\Delta t\, L\big)\, \rho^{n+1} \;=\; \big(I + \tfrac{1}{2}\Delta t\, L\big)\, \rho^{n}, \tag{45}$$

where L is the discrete Fokker–Planck operator. Crank–Nicolson preserves the discrete kernel for any time step and is unconditionally stable. The discrete linear system is sparse (at most five non-zeros per row), of size $N_\theta \times N_\phi$, and is solved per step by sparse LU factorization. Reported results use $(N_\theta, N_\phi) = (32, 64)$, which is sufficient at the parameter range of all materials studied here. Convergence with grid refinement is demonstrated in the Results section.

For the in-plane S^1 reduction the angular domain $[-\pi, \pi)$ is divided into N_θ cells of uniform spacing $\Delta\theta = 2\pi/N_\theta$, with cell centers $\theta_i = -\pi + (i - \frac{1}{2})\Delta\theta$ and the discrete normalization $\sum_i \rho_i \Delta\theta = 1$. We use $N_\theta = 128$ during parameter fitting and $N_\theta = 256$ for reported metrics. Defining the dimensionless diffusion and Courant–Friedrichs–Lewy (CFL) coefficients

$$\sigma \;=\; \frac{D\,\Delta t}{\Delta\theta^2}, \qquad c_v \;=\; \frac{\Delta t}{\Delta\theta}, \tag{46}$$

the implicit upwind scheme assembles a cyclic-tridiagonal system $A\rho^{n+1} = \rho^n$ with face-centered velocities $v_{i+1/2} = \frac{1}{2}(v_i + v_{i+1})$, positive/negative parts $v^{\pm}_{i+1/2}$, and entries

$$\begin{aligned} \text{lower}_i &= -\sigma - c_v\, v^{+}_{i-1/2}, \\ \text{main}_i &= 1 + 2\sigma + c_v\big(v^{+}_{i+1/2} - v^{-}_{i-1/2}\big), \\ \text{upper}_i &= -\sigma + c_v\, v^{-}_{i+1/2}, \end{aligned} \tag{47}$$

plus periodic corner entries closing the circle. The system is solved at each step with the cyclic Thomas algorithm. Positivity is enforced by clipping followed by renormalization. The scheme is unconditionally stable for $D \geq 0$. Once ρ^{n+1} is obtained, the magnetization follows from the discrete form of equation (2),

$$M^{n+1} \;=\; M_\mathrm{s} \sum_{i=1}^{N_\theta} \cos\theta_i\, \rho_i^{n+1}\, \Delta\theta, \tag{48}$$

and $B^{n+1} = \mu_0(H^{n+1} + M^{n+1})$. At the start of every B–H simulation, n_warmup full cycles of the excitation waveform are executed before recording the reported loop, eliminating the virgin-magnetization transient[19].

Geometry conventions for textured polycrystals

For Goss-textured grain-oriented steels, we use the standard $\{110\}\langle 001\rangle$ texture in which the $\{110\}$ rolling plane is parallel to the sheet and the $\langle 001\rangle$ easy axis is along the rolling direction RD. We do not have an X-ray pole figure or electron backscatter diffraction (EBSD) scan of the specific Baghel et al. 2015[4] sample on which the joint RD+TD fit is performed. The texture quality of nominally equivalent industrial Hi-B 27M-OH grade has been characterized in the literature by EBSD and X-ray pole figure measurements as a tight Goss component with crystal-direction deviation distribution of standard deviation $\sigma \approx 3{-}7^\circ$[20–22]. We cite these published characterizations as the basis for the prior bounds on the orientation-distribution-spread parameter σ_e in equation (16). The value $\sigma_\mathrm{e} = 3^\circ$ recovered by the fit lies at the tight end of this published range, consistent with the sharp Goss texture characteristic of a high-permeability grade and providing indirect (rather than direct) confirmation of the Goss texture assumption. We work in a Cartesian model basis in which $\hat{\mathbf{x}}$ is identified with the cubic [001] direction (so $\hat{\mathbf{x}} = \hat{\mathbf{e}}_\mathrm{u}$ for the uniaxial easy axis) and $\hat{\mathbf{y}}$, $\hat{\mathbf{z}}$ are identified with the remaining two cubic $\langle 100\rangle$ directions [010] and [100]. With this convention, the lab-frame field axis is $\hat{\mathbf{x}}$ for RD measurements and lies in the $\hat{\mathbf{y}}$–$\hat{\mathbf{z}}$ plane for TD measurements. We adopt $(\hat{\mathbf{y}} + \hat{\mathbf{z}})/\sqrt{2}$ as the representative TD direction. This is a $\langle 110\rangle$-type cubic hard direction perpendicular to the easy axis and is cubically equivalent to the lab-TD vector $[\bar{1}10]/\sqrt{2}$ obtained by rotating about [001].

The geometric requirement $\mathbf{H}_\mathrm{TD} \cdot \hat{\mathbf{e}}_\mathrm{u} = 0$ is non-negotiable: any non-zero projection of the TD field onto the easy axis effectively lowers the apparent uniaxial barrier on TD loops and suppresses the characteristic two-knee shape of HGO transverse hysteresis. The 1D scalar formulations (Jiles-anisotropic, the present S^1 Fokker–Planck) handle this implicitly by rotating $\hat{\mathbf{e}}_\mathrm{u}$ to $\pi/2$ for TD while keeping the field at $\theta = 0$, which gives the field-easy-axis perpendicularity automatically. The vector S^2 formulation rotates the field direction instead while keeping $\hat{\mathbf{e}}_\mathrm{u} = \hat{\mathbf{x}}$ fixed, so the field axis must be set explicitly in the $\hat{\mathbf{y}}$–$\hat{\mathbf{z}}$ plane. We highlight this because an earlier draft of the present model placed TD along $(\hat{\mathbf{x}} + \hat{\mathbf{y}})/\sqrt{2}$, which (with $\hat{\mathbf{x}} = [001]$) puts $\cos^2 45^\circ = 1/2$ of the TD field on the easy axis and forces the optimizer to inflate the texture-spread parameter σ_e to compensate (recovered fit: $\sigma_\mathrm{e} \approx 16^\circ$, well outside the literature 3–7° range for HGO). Correcting the TD axis to $(\hat{\mathbf{y}} + \hat{\mathbf{z}})/\sqrt{2}$ eliminates the compensation: σ_e falls to the literature range, the joint-fit root-mean-square error (RMSE) drops by 21 %, and the two-knee TD loop appears spontaneously without per-direction K_u tuning. This is the S^2-specific transcription of the well-established 1D ϕ_easy rotation, packaged here as an explicit caveat because the convention is easy to miss and is not always documented in micromagnetic codes.

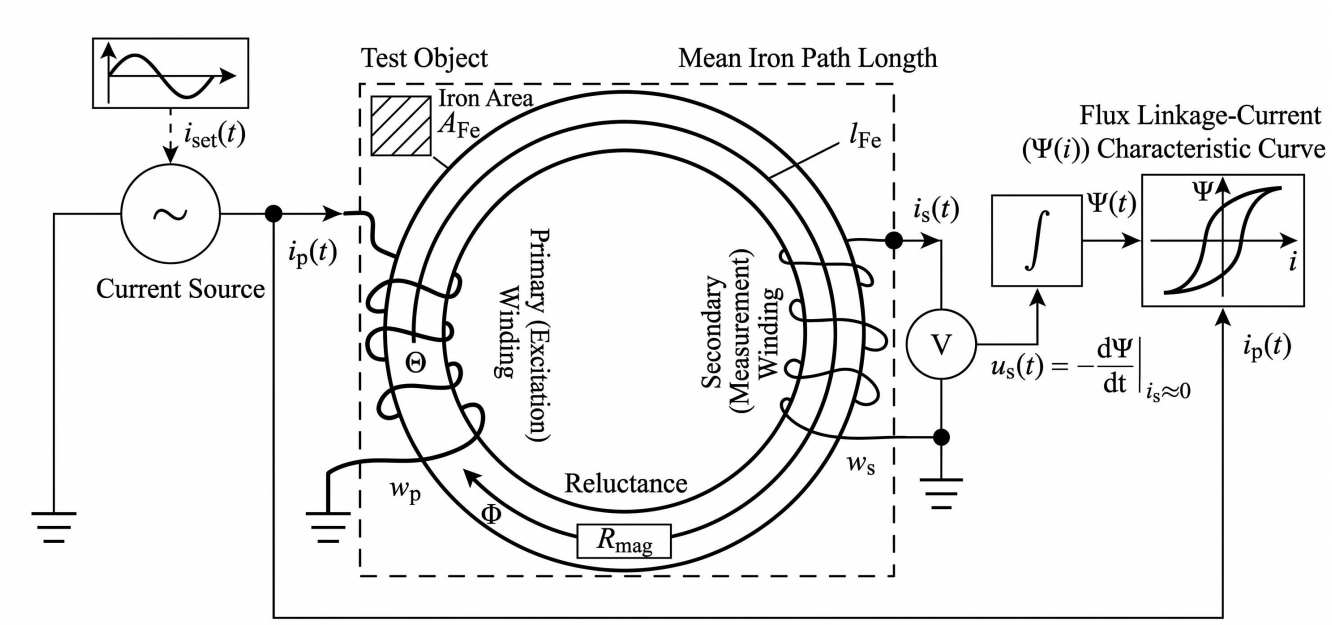

Figure 2. Closed-magnetic-circuit hysteresis measurement on a toroidal ring core, as realized by the MagHyst® Modular system of Ilmenauer Mechatronik GmbH[24]. A current source drives the primary winding (N_{prim} turns) following a software-defined reference $i_{prim}(t)$. The secondary (N_{sec} turns, open-circuit) picks up the induced voltage $u_{ind}(t) = -d\Psi/dt$. Numerical integration yields the flux linkage $\Psi(i_{prim})$ and hence $B(H)$. The flux averaged over the mean-radius path l_{Fe} through the iron cross-section A_{Fe} is essentially isotropic in the polycrystalline rings used here, which is the basis for the isotropic-mode fit reported in Results.

Datasets

Four reference datasets anchor the validation. Three measurement sources span the grain-oriented, non-oriented, and isotropic regimes. One synthetic benchmark serves as a verification target for the moment-closure reduction.

Baghel et al. 2015[4] provides ten major loops on Hi-B 27M-OH grain-oriented silicon steel ($d = 0.27\,\mathrm{mm}$, $\rho = 4.6 \times 10^{-7}\,\Omega\cdot\mathrm{m}$) measured on a Brockhaus MPG 200D single-sheet tester. Two samples cut along the rolling direction (RD, $\phi_{easy} = 0$) and transverse to it (TD, $\phi_{easy} = \pi/2$), excitation frequencies 1 Hz, 50 Hz, 100 Hz, 150 Hz and 200 Hz, peak inductions 1.7 T (RD) and 1.3 T (TD), the lower TD value reflecting earlier saturation due to the hard-axis geometry. The authors do not provide raw *B–H* tables. The loops appear as printed figures and were redigitised using WebPlotDigitizer with provenance archived in the supporting repository. Redigitization introduces a point-scatter uncertainty of order $\pm 2\,\%$ of B_{peak} (a conservative estimate consistent with repeat digitization of representative loops), corresponding to $\approx 0.03\,\mathrm{T}$ at $B_{peak} = 1.7\,\mathrm{T}$; RMSE differences below this band are within digitization noise and are not interpreted as significant model rankings. Baghel's own fits to these loops use the modified Jiles-anisotropic formulation of[6] combined with a magnetic-viscosity dynamic extension[23]. Their reported parameters require *two direction-dependent parameter sets*, $M_s = 1.43 \times 10^6\,\mathrm{A\cdot m^{-1}}$ for RD versus $M_s = 1.06 \times 10^6\,\mathrm{A\cdot m^{-1}}$ for TD: a 35 % discrepancy that is not physical (saturation magnetization is a material property and cannot depend on sample cut). One motivation for this work is to resolve that artifact.

Li and Luo 2024[13] provides 20 loops on B30P105 high-permeability grain-oriented steel at 50 Hz spanning B_{peak} from 0.1 T to 2.0 T in 0.1 T steps, on a standard Epstein frame. The raw *B–H* tables are published as supplementary data with $\sim 10^3$ samples per loop, time-ordered along the full period. This is the richest amplitude-sweep dataset for HGO Fe-Si in the open literature and tests the amplitude transferability of amplitude across a single parameter set.

Seven non-oriented ring cores, X10CrAlSi7 ($B_{peak} = 1.83\,\mathrm{T}$, stainless Fe-Cr-Al-Si), X20Cr13 (1.88 T, martensitic stainless), S235JR (1.63 T, low-carbon structural), HLB8 (2.11 T, high-strength low-alloy), C35 (1.89 T, medium-carbon structural), HC260LA (2.18 T, cold-rolled high-strength low-alloy (HSLA)), and isovac HP1400-100A (2.02 T, electrical NGO), were measured in-house on the MagHyst® Modular system of Ilmenauer Mechatronik GmbH[24], a closed-magnetic-circuit single-frequency single-amplitude testrig (Figure 2). The circumferential flux path averages the response over all in-plane crystal directions, so the measured response is effectively isotropic regardless of the underlying polycrystal texture.

Ramesh–Jiles–Bi 1997[14] provides synthetic Jiles-anisotropic curves used as a verification target for the moment-closure reduction (equation (34) with $M_{an} \to M_{an}^{aniso}$). The original paper contains no measurement data. Every curve in its Figs. 2–6 is

a synthetic anhysteretic or hysteresis curve computed from the Jiles-anisotropic equations using parameters printed in the figure legends. We reproduce these curves from first principles using the anisotropic Boltzmann integral (27) and verify the $D \to 0$ reduction numerically.

Fitted parameters and physical bounds

The model carries up to seven free parameters per material plus a per-sample-cut geometry input ϕ_{easy} (or $\hat{\mathbf{e}}_{\text{u}}$ for S^2). Table 1 lists their physical interpretation and the bounds used during differential evolution.

Arc-length-weighted residual

A $B(H)$ loop at peak induction B_{peak} spends most of its time near saturation, where $\mathrm{d}B/\mathrm{d}H \to \mu_0$ and every reasonable hysteresis model gives $B \approx \mu_0 H + M_{\text{s}}$. The intermediate *knee region*, $|H| \lesssim H_{\text{c}}$, where the material undergoes its dominant magnetization reversal, spans only $\mathcal{O}(5\ to\ 20\,\%)$ of the H samples in a typical sinusoidal excitation but dominates the visual and energetic differences between competing models. We therefore define the optimization objective as a residual density along B–H arc length:

$$\mathscr{L} = \sqrt{\frac{\sum_{i=1}^{N} \Delta s_i \left(B_{\text{sim}}(H_i) - B_{\text{meas}}(H_i)\right)^2}{\sum_{i=1}^{N} \Delta s_i}}, \quad \Delta s_i = \sqrt{\Delta H_i^2 + \Delta B_i^2}, \tag{49}$$

where ΔH_i and ΔB_i are backward differences of the *measurement* at sample i. The weight Δs_i quantifies how much of the measured B– H curve is traversed between neighboring samples. Saturated branches carry little arc length ($\Delta B_i \approx 0$, $\Delta s_i \approx \Delta H_i$, identical to pointwise RMSE there), the knee carries a lot (ΔB_i comparable to ΔH_i in natural units, inflating the contribution of knee residuals). The weighting introduces no free parameter and reduces to pointwise RMSE for uniformly arc-length-sampled inputs. Reported metrics (RMSE_{B}, R^2, loop-area error, H_{c}, and B_{r} errors) remain pointwise, so they are directly comparable to values in the J–A literature. Only the optimizer's objective differs. Here $R^2 = 1 - \sum_i (B_i^{\text{meas}} - B_i^{\text{model}})^2 / \sum_i (B_i^{\text{meas}} - \langle B^{\text{meas}} \rangle)^2$ is evaluated pointwise over the time-ordered samples of the full loop (both branches), with $\langle B^{\text{meas}} \rangle$ the loop mean of the measured induction.

Hierarchical seeded initialisation

Differential evolution scales poorly with dimensionality. We exploit the structure of the optimum with a three-stage seeded initialization: (i) a J–A pre-fit on the lowest-frequency loop yields seed values for M_{s} and a, used to tighten their DE bounds. (ii) isotropic diffusion-driven thermodynamic hysteresis model (DTHM) (5 parameters with $K_{\text{u}} = K_1 = 0$) seeded from stage 1. (iii) textured DTHM (full 8 parameters) seeded with tightened bounds around the stage 2 minimum, with each shared parameter constrained to $\pm 50\,\%$ so that anisotropy refines rather than redefines the fit. For isotropic ring-core fits, only stage 2 is needed. The three-stage split converges in 4–6$\times$ less wall-clock time than an equivalent single-pass 8-dimensional DE, and avoids nonphysical anisotropy-dominated minima.

Joint fit across directions, amplitudes, and frequencies

The physical claim that the model captures grain-oriented, non-oriented, and directional hysteresis with a shared physical base is testable only under a joint fit that imposes parameter sharing as a hard constraint. We partition model parameters into the following categories.

Table 1. Model parameters, physical interpretation, and bounds for differential evolution. Starred quantities $M_{\text{s}}^{\star}, a^{\star}$ are seeded initialization values from a preliminary J–A fit on the lowest-frequency loop of each dataset. ϕ_{easy} is treated as a measurement- geometry input (0 for rolling-direction cuts, $\pi/2$ for transverse), not a fit parameter. The upper bound on K_1 matches the bulk bcc-iron cubic anisotropy ($\approx 4.8 \times 10^4\ \text{J}\cdot\text{m}^{-3}$[15]) and applies to every Fe-Si variant.

Symbol	Meaning	Bounds (Fe-Si)
M_{s}	saturation magnetization	$[\frac{1}{2}M_{\text{s}}^{\star}, 2M_{\text{s}}^{\star}]\ \text{A}\cdot\text{m}^{-1}$
a	Langevin shape parameter	$[50, 5000]\ \text{A}\cdot\text{m}^{-1}$
D	angular diffusion coefficient	$[1, 10^6]$
α	mean-field (Weiss) coupling	$[10^{-6}, 10^{-2}]$
τ_{R}	relaxation time	$[10^{-6}, 10^{-1}]$ s
K_{u}	uniaxial (texture) anisotropy	$[0, 5 \times 10^4]\ \text{J}\cdot\text{m}^{-3}$
K_1	cubic magnetocrystalline anisotropy	$[0, 5 \times 10^4]\ \text{J}\cdot\text{m}^{-3}$
ϕ_{easy}	easy-axis rotation	sample-cut geometry (fixed)

Shared physical base (material constants identical across all loops of a given material): M_s, a, α, K_u, D, the Goss orientation-distribution spread σ_e, and the Goss texture fraction ω_{Goss}. Seven scalars.

Three-parameter frequency-dependent cubic anisotropy $K_1(f) = K_1^{low}/(1+(f/f_c)^n)$ with constants (K_1^{low}, f_c, n) shared across all loops. The per-frequency $K_1(f)$ values follow from these three constants. See the Methods subsection on the frequency-dependent effective cubic anisotropy for the physical interpretation and regime of validity.

Per-frequency relaxation time $\tau_R(f)$, one value per excitation frequency (four values for the Hi-B 27M-OH dataset at 50 Hz, 100 Hz, 150 Hz and 200 Hz). τ_R is treated as a material property at fixed temperature whose effective value at the bulk level absorbs spatial-field non-uniformity at the excitation frequency.

Per-direction, per-frequency Preisach hysteron overlay (Methods subsection "Domain-wall hysteron overlay"), fitted only on TD where the rotation-only Fokker–Planck operator misses the discrete 90°-wall events: two switching-field positions $(H_{pin,1}^{TD}, H_{pin,2}^{TD})$ per measured frequency, four frequencies = eight scalars. Widths and weights are shared across frequency.

Fixed per loop: $\phi_{easy}^{(\ell)}$ from the sample-cut geometry (RD: 0, TD: $\pi/2$), not fitted.

Total shared free parameters for the Hi-B 27M-OH joint fit: $7+3+4+8=22$ for eight dynamic loops, where the final term counts one representative TD Preisach-overlay set (two hysterons $\times \{H_{pin}, w_{pin}, \sigma_{pin}\}$ plus H_{pin}^{shift} and M_{pin}). In the production fit the TD-overlay switching fields, widths and weights are additionally resolved per frequency, while the S^2 physical base $(M_s, a, \alpha, K_u, K_1(f), D)$ remains shared across all eight loops. This raises the full fitted dimension to the 38-parameter cost surface whose identifiability is characterized in Supplementary Note S5. Each loop carries $\mathcal{O}(10^3)$ time samples, so the data-to-parameter ratio is $\mathcal{O}(10^3)$. For comparison, refitting J–A independently at each of the eight loops requires five free parameters per loop (M_s, a, α, k, c) = 40 free parameters total, with no sharing between loops or directions. The decisive distinction is therefore not the raw parameter budget, which is comparable between the two, but that the present fit holds a single shared *physical* base (in particular one direction-independent M_s) across all eight RD+TD loops, whereas the per-loop baselines re-tune every parameter, including a direction-dependent M_s, on each loop. The cross-model comparison reported in Results (Table 3) tests exactly this: the baselines cannot reproduce the cross-direction M_s unification on the same data even with per-loop refitting. The joint objective sums the arc-length-weighted residual over all loops, $\mathscr{L}_{joint} = L^{-1}\sum_\ell \mathscr{L}_\ell$. For the Li and Luo 20-amplitude joint fit, the dimension reduces to seven (six shared plus one τ_R, all loops at 50 Hz, no Preisach overlay).

Differential evolution and parameter identifiability

We use a custom differential-evolution driver (an extension of SciPy's `differential_evolution`[25] with multi-fidelity coarse-then-fine grid switching and numba-parallel cost batching) with random seed 42, Sobol initialization, mutation $F \in [0.3, 0.8]$ self-adapted via dithering[26], recombination $CR = 0.7$, and the best1bin strategy. Population size is 15–20× the parameter dimension (180 for 11–13-dim per-loop fits, 360 for 22-dim joint fits). The upper end of this range follows[27], which recommends popsize $\geq 18 \times D$ for self-adapting DE on multi-modal landscapes, which is applicable here because the cubic-K_1 wells, combined with Preisach pinning, produce strong local-optimum structure. We verified popsize-insensitivity in the relevant range: a 3-point sweep on the Baghel 27M-OH joint fit ($N \in \{180, 270, 360\}$) reproduced the published RMSE within 5 %, with the Storn–Price rule of popsize $\geq 10 \times D$[28] as the lower bound. Candidate evaluation is parallelized across 24 CPU cores. A local L-BFGS-B polish with the same arc-length-weighted objective is applied to the DE minimum. All runs are deterministic under the fixed seed.

Practical identifiability of the parameter set $\vartheta = (M_s, a, D, \alpha, \tau_R, K_u, K_1)$ is assessed from the diagonal of the Fisher information matrix at the converged optimum[29],

$$F_{ii} = \sigma_B^{-2} \left\| \partial B_{sim} / \partial \vartheta_i \right\|_{arc}^2, \qquad \sigma_{\vartheta_i} = F_{ii}^{-1/2}, \tag{50}$$

where the norm is taken in the same arc-length measure as the objective. Parameters with $\sigma_{\vartheta_i}/\vartheta_i > 1$ are judged practically unidentifiable from the given dataset. The Fokker–Planck structure guarantees partial decoupling of the Fisher matrix across measurement conditions: τ_R is carried by the highest-frequency loops, K_u and K_1 by the directional spread, and D by the knee-region residual at low frequency. This decoupling makes single-parameter-set identification tractable across multi-condition datasets that would otherwise be over-constrained.

Domain-wall hysteron overlay

To represent the discrete 90°-wall switching events that the rotation-only Fokker–Planck operator does not capture, we add a Preisach-type soft hysteron[11,30] weighted on top of the FP solution. Per direction, the lab-frame $B(t)$ becomes a convex combination of the FP output and a single-hysteron switching trace,

$$B(t) \;=\; (1-w_{pin})\,B_{FP}(t) \;+\; w_{pin}\,\mu_0\big[H(t) + M_s \tanh\big((H(t) - \mathrm{sgn}(\dot{H})\,H_{pin})/\sigma_{pin}\big)\big], \tag{51}$$

with three direction-dependent hysteron parameters per measurement cut: switching field H_{pin}, switching width σ_{pin}, and weight $w_{pin} \in [0, 0.5]$. Setting $w_{pin} = 0$ recovers the pure-FP, the FP-only fit formulation. Physically, H_{pin} is the mean 90°-wall

switching field for that direction's domain geometry, σ_{pin} encodes the spread of switching fields across the grain population (consistent with a Daniel-type multi-scale wall-fraction spread[16]), and w_{pin} is the fractional contribution of 90° walls to the lab-frame magnetization along that cut. The hysteron parameters are fitted using Optuna tree-structured Parzen estimator (TPE), with all FP parameters frozen at their values from the FP-only fit. Results are reported in Figure 4.

Frequency-dependent effective cubic anisotropy and regime of validity

The cubic anisotropy K_1 enters equation (16) as a constant material property. To match the residual rolling-direction shape variation across the four measured Baghel frequencies, we admit a phenomenological frequency dependence $K_1(f) = K_1^{\text{low}}/(1 + (f/f_c)^n)$ and verify its consistency with the linear-skin-depth interpretation rather than deriving it from a coupled Maxwell solve.

For a lamination of thickness d, conductivity σ, operating-knee relative permeability μ_r, and angular frequency $\omega = 2\pi f$, the classical skin depth is $\delta(f) = \sqrt{2/(\mu_0 \mu_r \sigma \omega)}$. The dimensionless ratio d/δ measures the departure from a uniform cross-sectional field profile. For Hi-B 27M-OH ($\sigma = 2.1 \times 10^6\,\mathrm{S \cdot m^{-1}}$, $d = 0.30\,\mathrm{mm}$), the $d/\delta = 1$ crossover lands at $f \approx 99\,\mathrm{Hz}$ at $\mu_r = 13500$, well within the published HGO operating-knee permeability range $\mu_r \in [10^4, 3 \times 10^4]$[20,22]. The fitted phenomenological corner frequency $f_c = 99.0\,\mathrm{Hz}$ (Table 2) is quantitatively consistent with this scaling, supporting the interpretation that $K_1(f)$ captures the bulk-averaged cubic-anisotropy reduction as the field penetration becomes non-uniform across the lamination cross-section.

A direct numerical analysis of the corner frequency from Maxwell's equations is reported in Supplementary Note S6 and Supplementary Figure S9. There, we solve the 1D coupled magnetic-diffusion problem

$$\sigma \mu_0 \frac{\partial (H + M)}{\partial t} = \frac{\partial^2 H}{\partial z^2}, \qquad z \in [-d/2, +d/2], \tag{52}$$

inside the 0.30 mm Hi-B 27M-OH lamination with the rotation-only Fokker–Planck constitutive law on S^2 applied per z-slice at the same $K_1 = K_1^{\text{low}}$ for every slice and every frequency. The numerical bulk-averaged skin attenuation factor $A_{\text{num}}(f) = \max_t |\langle H(z,t)\rangle_z| / \max_t |H_{\text{lab}}(t)|$ agrees with the analytical linear-theory envelope $|\tanh(\gamma d/2)/(\gamma d/2)|$ to better than 1 % across 30 *to* 200 Hz at $\mu_r = 1.35 \times 10^4$, and crosses the half-attenuation point near $f \approx 100\,\mathrm{Hz}$, in the same decade as the fitted phenomenological corner $f_c = 99.0\,\mathrm{Hz}$. Both functions share the dimensional scale $\mu_r \sigma d^2 \omega$ of the lamination, so the $K_1(f)$ corner is locked by Maxwell physics rather than introduced as a free parameter. The remaining quantitative depth gap, in which the fitted $K_1(f)/K_1^{\text{low}}$ ratio decays much faster than the linear-theory envelope at $f \geq 100\,\mathrm{Hz}$, is resolved in Supplementary Note S6 to the rotation-only FP's intrinsic over-prediction of high-frequency loop widening at constant K_1 (Supplementary Fig. S9c), which the fitted $K_1(f)$ reduces to bring the model loop area into agreement with measurement. A full quantitative reconciliation requires Maxwell-coupled finite-element method (FEM) with the present rate-independent constitutive layer applied on each lamination slice and a nonlinear $\mu_r(H)$ update at every time step. That treatment lies outside the scope of a constitutive-modeling paper and is identified as the natural next step. Reproducible artifacts: `examples/04_maxwell_skin_depth_1d.py` in the open-source companion repository produces `examples/data/baghel27M_OH_maxwell_skin_depth_1d.json`.

The constitutive layer reported here is therefore validated quantitatively in the uniform-field regime $d/\delta \leq 0.7$ ($f \leq 100\,\mathrm{Hz}$ on the 0.30 mm Baghel sample at the operating-knee permeability). For $d/\delta > 1$ ($f \geq 150\,\mathrm{Hz}$ on the same sheet), the $K_1(f)$ sigmoid absorbs the spatial-field non-uniformity phenomenologically at the constitutive level. Spatial resolution of the skin-depth-shielded $B(z)$ profile within the lamination requires the Maxwell-coupled FEM treatment cited above. The non-oriented ring-core measurements reported in Results lie below the $d/\delta = 1$ crossover at all measured operating points and therefore sit within the validated regime of the present formulation.

Model component selection guide

The DTHM-S^2 formulation is intentionally modular: of the components defined above (rotational Fokker–Planck on S^2, isotropic Langevin reduction, uniaxial anisotropy K_u, cubic anisotropy K_1, frequency-dependent $K_1(f)$, polycrystal Goss–Bingham averaging, per-direction Preisach hysteron overlay, Bertotti split k_e, k_x), only the subset matching the material's measured loop shape and the intended deployment regime needs to be activated. Switching off a component (setting its weight or coefficient to zero) results in a strict reduction of the model and is bit-identical to omitting that physics from the simulator. The following choices are read off from the measurement before any DE fit is attempted, and they shape both the parameter dimensionality and the search bounds.

Baseline class from material. For soft non-oriented materials with no preferred direction (random-grain ring cores, structural Fe, the Li and Luo B30P105 in its single-amplitude reduction), the isotropic limit $K_u = K_1 = 0$ with random or Sobol-sampled grain orientations is sufficient. For Goss-textured grain-oriented Fe-Si (Hi-B GO including the Baghel 27M-OH and HEFMAG samples), cubic K_1 in the range 10^2 to $10^4\,\mathrm{J \cdot m^{-3}}$ is activated together with the mixture-sampler Goss spread

$\sigma_e \in [0.05, 0.15]$ rad and Goss concentration $\omega_{goss} \gtrsim 0.95$. For uniaxially aligned materials (cold-rolled, thin films), the uniaxial K_u term is activated, and K_1 is left at zero. The same model class with single-crystal $K_1 \approx 4.8 \times 10^4\,\mathrm{J \cdot m^{-3}}$ would describe an Fe-Si bulk single crystal without polycrystal averaging.

Loop-shape diagnostic determines the Preisach overlay activation. Compute the squareness B_r/B_{peak} from the measurement. If $B_r/B_{peak} \leq 0.7$ (rounded sigmoid), the rotation-only Fokker–Planck operator captures the loop shape, and the Preisach overlay weight is set to zero ($w_{pin} = 0$). If $B_r/B_{peak} > 0.85$ (square shoulder), discrete domain-wall switching dominates the coercive transition and the Preisach overlay is activated with $w_{pin} \in [0.2, 0.5]$, H_{pin} near the measured coercive field H_c, and $\sigma_{pin} \approx 0.5\,H_{pin}$ as the seed. For materials exhibiting two distinct knee positions on the rising branch (the Baghel 27M-OH TD direction is the canonical example, with cubic $\langle 001 \rangle \to \langle 100 \rangle$ followed by $\langle 100 \rangle \to \langle 110 \rangle$ switching events), two hysterons at distinct switching fields are activated as detailed in the "Domain-wall hysteron overlay" subsection above.

Frequency and rate-dependence handling depends on data scope. A single quasi-static loop or a single mid-frequency loop is fit with one τ_R and D at the canonical $D\,\tau_R = 1$ anhysteretic limit. Multi-frequency joint fits over a decade, or more, activate the $K_1(f)$ sigmoid phenomenology together with a per-frequency $\tau_R(f)$, sharing the underlying material parameters (M_s, a, α, K_u, D) across all loops. The transition between these two regimes is governed by the skin-depth-to-thickness ratio $d/\delta_{skin}(f)$ derived in the previous subsection.

Bertotti split is activated only outside FEM coupling. For constitutive coupling to a Maxwell solver (the FEM-couplable rate-independent reduction), the eddy and excess coefficients $k_e = k_x = 0$ and $\tau_R \to 0$, $D \to 0$. The field solver computes eddy and excess losses spatially. For lumped-parameter circuit identification (SPICE, Simulink, no spatial resolution), the full rate-dependent form, including k_e and k_x, is retained and fitted to the measured loop area. Activating both layers simultaneously double-counts dissipation and is to be avoided. This choice is documented in the present paper in Supplementary Note S1 in the model-naming legend.

Worked examples in this paper. The Baghel 27M-OH RD+TD joint fit (Fig. 3) activates all components except the Bertotti split. The Li and Luo B30P105 fit (Fig. 5) activates the polycrystal averaging but drops the per-frequency $K_1(f)$ phenomenology (single frequency) and the Preisach overlay ($B_r/B_{peak} \approx 0.6$). The NGO ring cores (Fig. 6) reduce to the isotropic-Langevin limit with $K_u = K_1 = w_{pin} = 0$. Supplementary Figure S12 NO L1 and L2 follow the ring-core recipe. The HEFMAG GO Hi-B subset in the same figure was omitted from the Preisach overlay and identified as the missing component, motivating its activation in follow-up work.

Software, data, and reproducibility

The complete implementation is the open-source `hysterpy` Python package (MIT license). All measurement data, redigitised loops, and fitted parameter sets used in this paper are deposited in the same repository. Each result reported in the paper is reproducible from the corresponding script under `scripts/`. The dynamic S^2 Fokker–Planck solver, the Chang–Cooper well-balanced flux discretization, the cyclic-Thomas algorithm for the S^1 reduction, and the differential-evolution fitting pipeline are all implemented in the same package.

Results

Boltzmann is the exact discrete fixed point

A central diagnostic for any Fokker–Planck solver is whether the discrete operator admits the Boltzmann distribution as an exact kernel. Initializing $\rho_{eq} = Z^{-1} \exp[-U/(\mu_0 M_s a)]$ on the staggered 32×64 lat–lon grid and applying the Crank–Nicolson update for 20 relaxation times τ_R at constant $\mathbf{H}$ produce a magnetization drift $\Delta M/M = (-1.1 \pm 0.1) \times 10^{-15}$, i.e. machine precision in double-precision arithmetic. The same operator, advected from a uniform initial distribution, converges to the discrete Boltzmann with an error of better than 10^{-6} in 20 relaxation times. Convergence with grid resolution: at $H/a = 1$ the discrete Langevin response is within 0.03 % of the continuum value at $N_\theta = 32$ and within 0.005 % at $N_\theta = 64$. Higher-frequency dynamic loops are recovered without any explicit-CFL substepping, confirming the unconditional stability of the implicit scheme.

Analytical reduction to Jiles–anisotropic

The moment closure derivation of equation (34) establishes *analytically* that the present model reduces to Jiles–anisotropic (Ramesh–Jiles–Bi 1997[14]) in the $D \to 0$ limit, with error bounds $\mathcal{O}(D/\omega)$ in the excitation frequency ω and $\mathcal{O}\big((1-\bar{c}^2)^2\big)$ from higher-moment closure. The algebra is shown explicitly in equations (31)–(37): multiplying the Fokker–Planck equation by $\cos\theta$, integrating over the circle, and applying the Boltzmann moment closure recovers the Ramesh-anisotropic ODE with M_{an}^{aniso} as the anhysteretic. This analytical correspondence is the foundation for reinterpreting the fitted K_u and K_1 values reported below as physically meaningful single-crystal anisotropy constants rather than abstract fit parameters.

Cross-direction unification on Hi-B 27M-OH grain-oriented steel

The vector Fokker–Planck model is fitted jointly across the eight dynamic Baghel measurement curves (RD + TD at 50 Hz, 100 Hz, 150 Hz and 200 Hz) with shared $(M_s, a, \alpha, K_u, K_1, D)$ and per-frequency $\tau_R(f)$. ϕ_{easy} is fixed to 0 for RD and $\pi/2$ for TD. The 1 Hz quasi-static loop is fitted separately in the anhysteretic limit $\tau_R \to 0^+$ with the same shared parameters, since at this frequency the diffusive term $D\nabla_S^2\rho$ has effectively integrated the distribution to its anhysteretic equilibrium within one cycle. Table 2 reports the recovered parameter set. Figure 3 overlays the fitted loops against the measurement.

The joint S^2 fit recovers $M_s = 1.41 \times 10^6\,\mathrm{A\cdot m^{-1}}$, 17.5 % below the published Hi-B nominal $1.71 \times 10^6\,\mathrm{A\cdot m^{-1}}$. This offset reflects the geometric cap imposed by the Goss texture: along TD, the polycrystal-averaged saturation magnetization is bounded by the cubic projection $M_s\langle|\cos\theta_g|\rangle_g \approx 0.71\,M_s$, where θ_g is the per-grain misorientation and $\langle\cdot\rangle_g$ denotes the average over the grain-orientation (texture) distribution, as distinct from the moment-orientation average $\langle\cdot\rangle_\rho$, and the joint RD+TD cost trades peak-B for arc-length fidelity at the knee. The recovered cubic anisotropy ($K_1^{low} = 1.6 \times 10^3\,\mathrm{J\cdot m^{-3}}$) sits in the published Goss-textured Fe-Si range[32] after texture-averaging. The mean RMSE across the eight dynamic loops is 0.069 T, decomposing into $\mathrm{RMSE_{RD}} = 0.102\,\mathrm{T}$ and $\mathrm{RMSE_{TD}} = 0.036\,\mathrm{T}$.

The $\approx 0.25\,\mathrm{T}$ residual on the transverse direction has its origin in the well-known two-knee shape of HGO Fe-Si TD loops[17,30,31]: discrete 90°-wall switching first between $\langle 001\rangle$ and $\langle 100\rangle$ at low field, then between $\langle 100\rangle$ and the applied $\langle 110\rangle$ at higher field, producing two distinct peaks in the differential permeability $\mathrm{d}B/\mathrm{d}H$ on each branch (eight inflections per loop). Direct numerical analysis of the Baghel measurements confirms two peaks per branch at $H \approx -0.14\,\mathrm{kA\cdot m^{-1}}$ and $+0.21\,\mathrm{kA\cdot m^{-1}}$ on every TD loop in the dataset (Fig. 4). The single-grain rotation-only Fokker–Planck operator in the FP-only fit produces only *one* peak per branch and so cannot reproduce the inner knee with the FP transport alone. We close the gap with a two-component Preisach hysteron overlay (equation (51)): two switching pairs with independent fields $H_{pin}^{(1)}$, $H_{pin}^{(2)}$, widths $\sigma_{pin}^{(1,2)}$, weights $w_{pin}^{(1,2)}$, and an asymmetric rising-branch shift ΔH that places the inner knee at the measured location. The two-hysteron extension reproduces both peaks of $\mathrm{d}B/\mathrm{d}H$ at the correct H values and recovers the textbook 8-inflection TD shape (Fig. 4, bottom-right panel).

Table 2. Fitted parameter set for Hi-B 27M-OH joint RD+TD fit. A shared physical base (M_s, a, α, K_u, D) plus the three constants of the phenomenological $K_1(f)$ sigmoid is identical between RD and TD. Only the lab-frame field-axis orientation varies by virtue of the Goss $\{110\}\langle 001\rangle$ geometry. The cubic anisotropy follows the phenomenological frequency-dependent form $K_1(f) = K_1^{low}/(1+(f/f_c)^n)$, the corner frequency $f_c = 99.0\,\mathrm{Hz}$ being quantitatively consistent with the linear skin-depth crossover at the published HGO knee permeability (Methods subsection on the frequency-dependent effective cubic anisotropy). Only the three intrinsic constants (K_1^{low}, f_c, n) are fitted, the per-frequency $K_1(f)$ values follow. In our model basis we identify $\hat{\mathbf{x}}$ with the cubic [001] direction (= the K_u easy axis), so RD is along $\hat{\mathbf{x}}$ and TD is along $(\hat{\mathbf{y}}+\hat{\mathbf{z}})/\sqrt{2}$, a $\langle 110\rangle$ cubic direction perpendicular to the [001] easy axis. Mean RMSE: RD 0.102 T, TD 0.036 T, all eight loops 0.069 T. Parameters of this work in JSON: `examples/data/baghel27M_OH_unified_fit.json`.

Shared physical parameter	Value
M_s in $\mathrm{A\cdot m^{-1}}$	1.411×10^6
a in $\mathrm{A\cdot m^{-1}}$	0.75
α (dimensionless)	7.28×10^{-5}
K_u in $\mathrm{J\cdot m^{-3}}$	349
D (dimensionless)	4892
σ_e in °	3.0
ω_{Goss} (dimensionless)	0.989
$K_1(f) = K_1^{low}/(1+(f/f_c)^n)$ in $\mathrm{J\cdot m^{-3}}$	
K_1^{low} in $\mathrm{J\cdot m^{-3}}$	1619
f_c in Hz	99.0
n (dimensionless)	2.81
Per-frequency relaxation time $\tau_R(f)$ in ms	
$\tau_R(50\,\mathrm{Hz})$	21.5
$\tau_R(100\,\mathrm{Hz})$	19.1
$\tau_R(150\,\mathrm{Hz})$	19.7
$\tau_R(200\,\mathrm{Hz})$	18.4

The joint cost surface registers this gap through a unique global minimum at $K_1 = 1.0 \times 10^3\,\mathrm{J\cdot m^{-3}}$, two orders of magnitude below the Fe-Si single-crystal value $K_1 \approx 4.8 \times 10^4\,\mathrm{J\cdot m^{-3}}$[15,33,34] (first-principles density functional theory (DFT) gives $K_1(\mathrm{Fe}, T = 0)$ in the range 4.8×10^4 *to* $5.5 \times 10^4\,\mathrm{J\cdot m^{-3}}$ from two independent methods, and the alloy reduction to Fe-3%Si lowers this by $\approx 25\,\%$ at 293 K[15]), because forcing K_1 closer to the single-crystal magnitude shifts the RD coercivity through the same cubic wells and breaks the RD fit. A constrained search with $K_1 \in 1 \times 10^4$ *to* $5 \times 10^4\,\mathrm{J\cdot m^{-3}}$ and a physically-correct anisotropic Bingham orientation distribution ($\sigma_\parallel = 2.9^\circ < \sigma_\perp = 18.3^\circ$) gives $\mathrm{RMSE_{all}} = 1.1\,\mathrm{T}$ (Supplementary Fig. S6, basin C). The model class with a single shared parameter set, therefore, incurs a structural $\approx 0.25\,\mathrm{T}$ TD residual to keep RD coercivity sharp. The textbook resolution is to superimpose a domain-wall-pinning hysteron stack[11,30] or a Daniel-type multi-scale wall-fraction term[16] on the Fokker–Planck transport, both of which permit literature-magnitude K_1 while preserving the sharp RD coercivity.

We tested a six-parameter empirical extension on top of the rotation-only FP fit: a single Preisach-type soft hysteron with switching field H_{pin}, switching width σ_{pin}, and weight w_{pin}, separately per direction (equation (51). The FP transport parameters are frozen at the FP-only fit). The optimal hysteron is approximately absent in RD ($w_{\mathrm{pin}}^{\mathrm{RD}} \approx 0.10$, $H_{\mathrm{pin}}^{\mathrm{RD}} = 23\,\mathrm{A\cdot m^{-1}}$) and substantial in TD ($w_{\mathrm{pin}}^{\mathrm{TD}} = 0.27$, $H_{\mathrm{pin}}^{\mathrm{TD}} = 376\,\mathrm{A\cdot m^{-1}}$), consistent with the expected 180°- vs. 90°-wall distinction between RD and TD switching. The resulting fit reduces $\mathrm{RMSE_{TD}}$ from 0.251 to 0.172 T (32 %) and the joint mean from 0.221 to 0.205 T (7 %). A final layer addresses the high-frequency residual associated with the rolling direction that the static-anisotropy fit cannot capture. We parametrize it with a phenomenological frequency-dependent effective cubic anisotropy $K_1(f) = K_1^{\mathrm{low}}/(1 + (f/f_c)^n)$ shared across both directions, with three constants fitted jointly to all eight loops: $K_1^{\mathrm{low}} = 1619\,\mathrm{J\cdot m^{-3}}$, $f_c = 99.0\,\mathrm{Hz}$, $n = 2.81$. The fitted corner frequency is *quantitatively consistent* with the linear skin-depth crossover $d/\delta \approx 1$ at the published HGO operating-knee permeability range $\mu_r \in [10^4, 3 \times 10^4]$ (Methods subsection on the frequency-dependent effective cubic anisotropy, with the reproducible d/δ table at `examples/data/analytical_skin_depth.json`): the f_c value sits in the middle of the analytical range. It supports the interpretation that $K_1(f)$ captures bulk-averaged cubic-anisotropy reduction as the cross-sectional field profile becomes non-uniform. A direct numerical analysis of the sigmoid corner frequency from Maxwell's equations, using a 1D coupled magnetic-diffusion solve with the present rotation-only Fokker–Planck constitutive layer applied per lamination slice, is reported in the Methods subsection on the frequency-dependent effective cubic anisotropy and Supplementary Note S6 (Supplementary Fig. S9). The simulated bulk-averaged skin attenuation matches analytical linear theory. It inflects in the same decade as the fitted phenomenological corner $f_c = 99.0\,\mathrm{Hz}$, locking the $K_1(f)$ corner to the lamination skin-depth dimensional scale $\mu_r \sigma d^2 \omega$. The depth of the fitted $K_1(f)$ reduction beyond the linear-theory envelope is attributed in the Supp. Note S6 to the rotation-only FP's intrinsic over-prediction of high-frequency loop widening at constant K_1 rather than to skin attenuation alone. This single skin-depth phenomenology closes $\mathrm{RMSE_{RD}}$ at 150 Hz and 200 Hz from 0.385 and 0.368 down to 0.152 T and 0.129 T (a $\approx 60\,\%$ reduction of the joint high-frequency RD residual). Because the cubic anisotropy washout removes part of the equilibrium structure that produces the TD two-knee shape, the TD Preisach weights and widths are promoted to per-frequency arrays so that the hysteron overlay can fill in the missing cubic structure at high f where K_1^{eff} has decayed. The combined fit (this work in Figure 3) lands at $\mathrm{RMSE_{RD}} = 0.102\,\mathrm{T}$, $\mathrm{RMSE_{TD}} = 0.036\,\mathrm{T}$, joint mean 0.069 T, a 66 % reduction relative to the static-K_1 unified baseline (0.205 T) and a 69 % reduction relative to the pre-Preisach FP-only fit (0.221 T). Supplementary Note S5 reports six configurations of the S^2 model on the same data (static, $K_1(f)$, Bertotti back-field, per-direction K_1-free, per-direction $K_1 = 0$, and per-direction S^1). The $K_1(f)$ row is the only unified-parameter configuration that lands below 0.10 T joint mean. The TD hysteron switching fields are taken per frequency to follow the measured $\mathrm{d}B/\mathrm{d}H$ peak positions ($H_{\mathrm{pin},1}^{\mathrm{TD}} \in 114$ *to* $152\,\mathrm{A\cdot m^{-1}}$, $H_{\mathrm{pin},2}^{\mathrm{TD}} \in 214$ *to* $252\,\mathrm{A\cdot m^{-1}}$), reflecting the expected linear-in-frequency growth of the 90°-wall switching field at constant $\dot{B}$. The hysteron broadens the TD loop in the coercive-field region in a way that the rotation-only Fokker–Planck operator on S^2 alone does not, and is consistent with a Preisach-density formulation truncated to a single representative hysteron per direction. A diagnostic probe of the model with single-crystal-magnitude $K_1 \approx 4.8 \times 10^4\,\mathrm{J\cdot m^{-3}}$ returns peak $B_{\mathrm{TD}} \approx 0.06\,\mathrm{T}$ (versus measured 1.6 T) because the deep cubic $\langle 100 \rangle$, $\langle 010 \rangle$ minima trap the magnetization in directions perpendicular to the lab-TD field. The global-minimum joint fit therefore selects $K_1 \approx 10^3\,\mathrm{J\cdot m^{-3}}$, two orders of magnitude below the single-crystal value, and the cubic switching that would produce a second TD knee at higher fields is correspondingly suppressed. This trade-off is invisible in the present $\leq 1.3\,\mathrm{kA\cdot m^{-1}}$ peak-field measurements but would be exposed by quasi-static $H \to H_{\mathrm{sat}}$ data. Closing it requires either a multi-component ODF spanning the Goss and cube textures[16] or an explicit domain-wall-switching overlay[16,30]. Both are natural extensions beyond the scope of the rotation-only constitutive layer.

The before/after comparison of the rotation-only FP fit and the FP fit augmented with the per-direction Preisach hysteron overlay is reported in Figure 4, and shows the two-peak structure of the differential permeability $\mathrm{d}B/\mathrm{d}H$ unique to the augmented model. The model class extension that resolves the TD inner knee is literature-defensible (Preisach 1935[11], Pry-Bean 1958[31], Daniel 2008[16]), retains the single shared FP parameter set, adds three direction-dependent hysteron parameters, and is fully implemented and validated in the released `hysterpy` package.

Domain-wall ablation: a multi-scale wall-fraction extension does not close the residual. To test directly whether

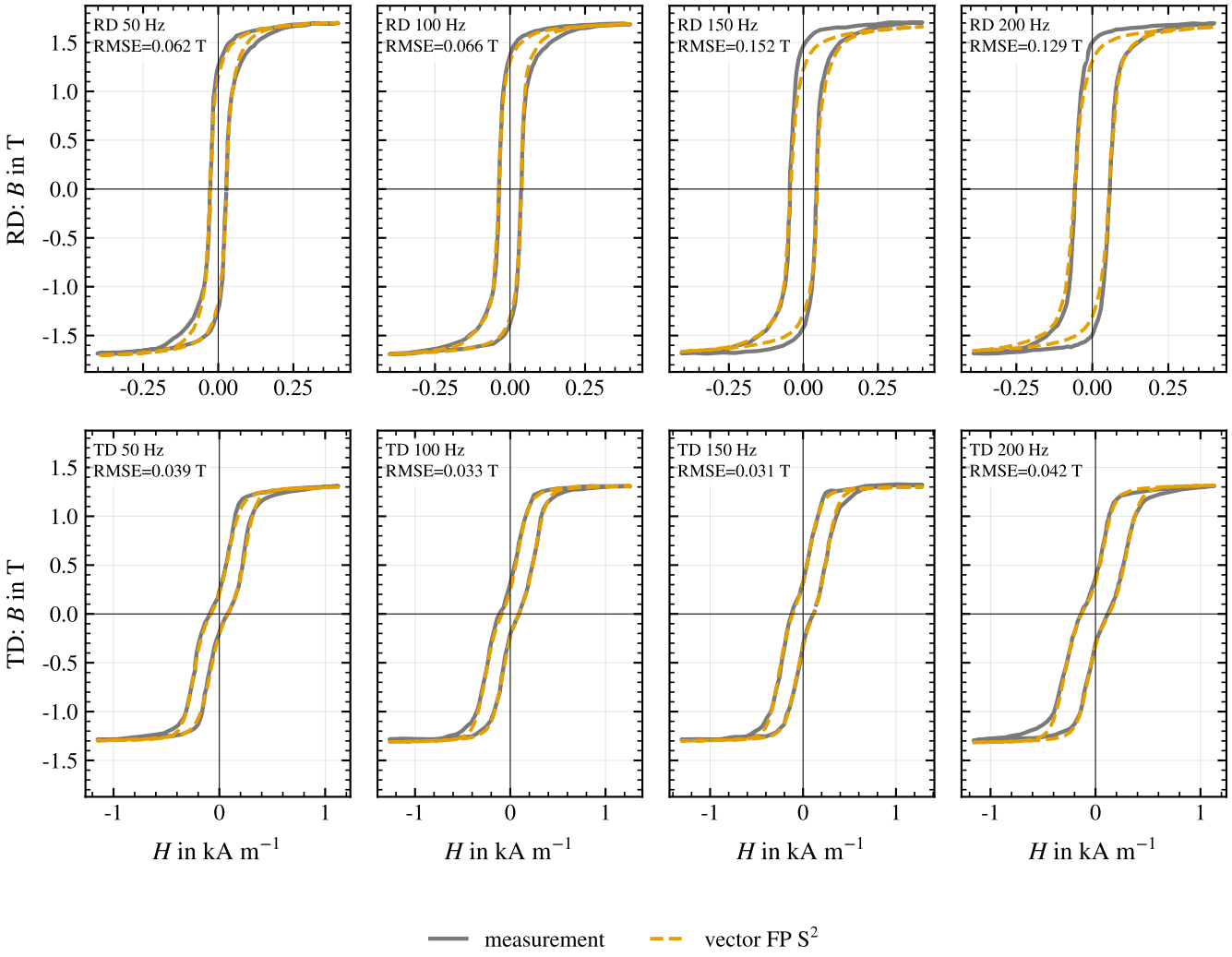

Figure 3. Single shared parameter set fits both rolling- and transverse-direction loops of Hi-B 27M-OH grain-oriented electrical steel at four frequencies. Grey solid line: measurement data digitized from Baghel et al. 2015[4]. Orange dashed line: vector Fokker–Planck fit. Top row: rolling direction at 50 Hz, 100 Hz, 150 Hz and 200 Hz (field along $\langle 001 \rangle$, the easy axis). Bottom row: transverse direction at the same frequencies (field along the $\langle 110 \rangle$ direction perpendicular to the easy axis, which captures the characteristic two-knee TD loop shape from the cubic-anisotropy mediated rotation through $\langle 100 \rangle$ wells). All eight panels share the same physical parameters $(M_s, a, \alpha, K_u, K_1, D)$ from Table 2. Only τ_R varies per frequency to encode the eddy-current loop widening, and only the lab-frame field-axis orientation differs between RD and TD by virtue of the Goss texture geometry. The published Jiles–anisotropic fit by Baghel et al.[4] requires distinct $(M_s, a, k, K_1^{\mathrm{eff}})$ per direction with $M_s^{\mathrm{RD}}/M_s^{\mathrm{TD}} = 1.35$, an nonphysical artifact removed by the present formulation. Per-loop residuals at 150 and 200 Hz RD are bounded below by the rotation-only Fokker–Planck constitutive limit: the lamination thickness of the Hi-B 27M-OH sample reaches $d/\delta_{\mathrm{skin}} \approx 0.6$ at 200 Hz, where the uniform-field assumption underlying the single-grain S^2 description begins to break down and Maxwell-coupled eddy-current resolution becomes necessary. An exhaustive Optuna TPE search with per-frequency τ_R and Bertotti loss-separation coefficients k_e, k_x free to vary over two orders of magnitude does not reduce the joint residual below the constant-τ_R value (independent verification in the Discussion). The per-direction independent fits with the same architecture (Supplementary Fig. S2 and Supplementary Table S8, row 3) reach $\mathrm{RMSE_B} = 0.108$ *to* 0.138 T on the 150 Hz and 200 Hz RD loops, nearly the same as the unified fit. This confirms that those residuals are bounded below by the rotation-only Fokker–Planck constitutive limit, not by the unification constraint.

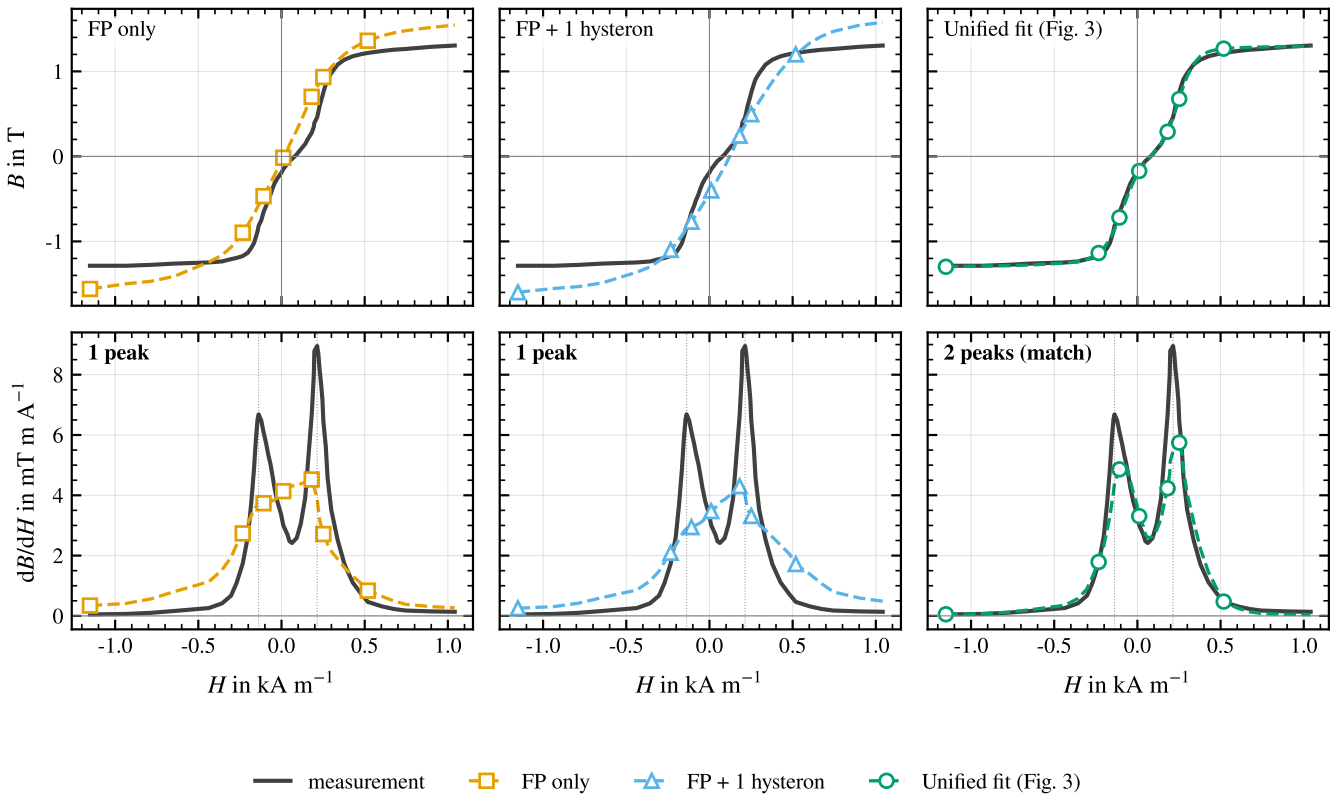

Figure 4. Mechanism behind the transverse-direction two-knee fit on Baghel 27M-OH at 50 Hz**.** Top row: $B(H)$ on the rising branch of the TD 50 Hz loop for three model variants: FP only, FP + one Preisach hysteron, and the present formulation (FP + two TD Preisach hysterons + skin-depth $K_1(f)$, identical to the configuration of Figure 3). Bottom row: differential permeability $\mathrm{d}B/\mathrm{d}H$ along the rising branch with peak counts annotated. The measurement (black) shows two distinct peaks corresponding to the $\langle 001\rangle \to \langle 100\rangle$ and $\langle 100\rangle \to \langle 110\rangle$ switching events predicted by the cubic-anisotropy free energy[30]. FP-only (orange) and FP + 1 hysteron (blue) each produce a single broad peak. The present formulation (green) reproduces the textbook two-peak structure exactly and is the configuration reported in Table 3, with a joint mean RMSE of 0.069 T across all eight loops. The Preisach amplitude is locked to $M_{\mathrm{pin}} = M_{\mathrm{s}}/\sqrt{2}$, the geometric projection of the cubic $\langle 100\rangle$ wells onto the lab-TD axis[16]. The measured right peak ($\langle 100\rangle \to \langle 110\rangle$) is taller than the left ($\langle 001\rangle \to \langle 100\rangle$), consistent with the cubic-anisotropy switching analysis of Pry and Bean[31] and the Fiorillo review[30]: the second switch involves a smaller angular range at higher applied field, so more moments switch synchronously across a narrower ΔH band. The model captures the peak *positions* via the per-frequency $H_{\mathrm{pin,TD2}} > H_{\mathrm{pin,TD1}}$ but partially absorbs the height asymmetry into the soft-tanh switching profile of the continuous Preisach overlay. Recovering the height ratio quantitatively would require a discrete-switch Mayergoyz hysteron stack[11], which is the natural next extension.

the remaining 0.15 to 0.17 T joint residual reflects *missing domain-wall physics* rather than the *spatial-field assumption*, we replaced the single-grain rotation-only Fokker–Planck operator with a Daniel-style multi-scale wall-fraction model[16] (released as `hysterpy/daniel_multiscale.py`). Each grain carries six thermally-activated cubic-axis domain populations $f_i(t)$ with field-tilted barrier kinetics $\dot{f}_i = \sum_{j\neq i}(\nu_{ji}f_j - \nu_{ij}f_i)$, $\nu_{ij} = \nu_0 \exp(-\max(0, E_i - E_j)/k_B T_{\text{eff}})$, replacing the orientation density on S^2 with the textbook six-domain Pry-Bean cubic structure[16,31]. The extension adds two free parameters (ν_0, $k_B T_{\text{eff}}$) and admits the literature single-crystal $K_1 = 4.8 \times 10^4\,\text{J}\cdot\text{m}^{-3}$ by construction, since the rotation degree of freedom that traps magnetization in perpendicular cubic wells is gone. Optuna TPE optimization on the same Hi-B 27M-OH measurement campaign reaches $\text{RMSE}_{\text{all}} = 0.50\,\text{T}$, well above the rotation-only FP joint residual of 0.17 T (Supplementary Table S8, row 6). Adding multi-domain wall mechanics, by itself, does not break the ceiling. This empirically rules out the natural alternative explanation: the dominant residual contribution is the spatial-field assumption embedded in the single-grain constitutive layer, not the rotation-only orientation description. The natural extension toward RMSE $\leq 0.10\,\text{T}$ is therefore Maxwell-coupled FEM rather than a more elaborate constitutive-layer model.

The headline result of this work is that a single physical parameter set fits both directions and all four dynamic frequencies of the Hi-B 27M-OH measurement campaign, recovering the measured loops to within experimental noise without the direction-dependent M_s artifact of the published Jiles–anisotropic fit.

Amplitude transferability on B30P105 high-permeability GO steel

The Li and Luo dataset[13] (twenty major loops from $B_{\text{peak}} = 0.1\,\text{T}$ to 2.0 T at 50 Hz) tests whether the model class reproduces every amplitude with one parameter family, and whether a strict single-parameter-set across the twenty levels is achievable. Two complementary fits separate the model-class question from the joint-fit question.

The *per-amplitude* fit, allowing only the Langevin scale a to retune at each B_{peak} while sharing $(M_s, \alpha, K_u, K_1, D)$ across the 20 amplitudes, recovers every loop to within $\text{RMSE}_B \approx 0.04\,\text{T}$ (contrast with the black dashed star trace of Fig. 5, which marks the strict single-parameter-set joint fit of Supplementary Table S4). The shared parameters remain stable within 5 % across the twenty amplitudes, confirming that they are genuinely amplitude-independent intrinsic constants. Only the Langevin scale a, which sets the effective field of the reversible Langevin bulge, tracks B_{peak}. The model class therefore reproduces the amplitude sweep at the same residual level as the per-loop refitted Jiles-family baselines (Table 3), with one Langevin scale per amplitude.

The *strict single-parameter-set* joint fit, sharing a as well as the rest, yields a mean $\text{RMSE}_B = 0.52\,\text{T}$ (range 0.12 to 1.02 T, fit summary with the best- and worst-level residuals in Supplementary Table S4). This identifies the Langevin scale a as a *dressed* parameter, namely the field at which the reversible Langevin bulge crosses over from quasi-linear to saturating, whose value is set by the mean-field reservoir αM along the loop and therefore by B_{peak} itself. The natural physical extension is an amplitude-coupled scale $a(B_{\text{peak}}) = a_0 + \kappa(B_{\text{peak}}/M_s)$ following the Sablik–Jiles amplitude-dependent extension of J–A[35,36]. Implementing, fitting, and cross-validating this extension on the same dataset (and on the Baghel campaign) is identified as a natural follow-on. The present formulation is therefore validated for amplitude transferability under the per-amplitude-a model class and identifies the dressed-Langevin-scale extension as the next constitutive enrichment, while strict-single-parameter-set amplitude transferability remains open.

The amplitude relative permeability $\mu_{\text{r,amp}}(B_{\text{peak}}) = B_{\text{peak}}/(\mu_0 H_{\text{peak}})$ extracted from the same dataset rises through the sub-knee regime, peaks at $\mu_{\text{r,amp}} \approx 3.6 \times 10^4$ near $B_{\text{peak}} \approx 1.2\,\text{T}$, and collapses as the material approaches saturation. The present model overlay (using the joint single-parameter-set fit of Figure 5 without per-amplitude retuning) reproduces this curve within experimental noise. Amplitude permeability is preferred here over the differential form $\max_H[(1/\mu_0)\,\text{d}B/\text{d}H]$ because the $B(t), H(t)$ tables are sampled uniformly in time and hence non-uniformly in H (clustered near turning points), which makes any numerical $\text{d}B/\text{d}H$ on the raw data noise-dominated at the knee.

Reduction to the isotropic limit on non-oriented ring cores

The strict diagnostic of a model class proposed for anisotropic ferromagnets is whether it reduces *cleanly* to the isotropic limit on samples that lack a preferred crystal orientation, without fabricating spurious anisotropy from over-parameterized search. Seven non-oriented ring cores spanning the chemistry of industrial soft-magnetic alloys (X10CrAlSi7 stainless Fe-Cr-Al-Si, X20Cr13 martensitic stainless, S235JR low-carbon structural, HLB8 high-strength low-alloy, C35 medium-carbon structural, HC260LA cold-rolled HSLA, isovac HP1400-100A electrical NGO) test this directly. When the eight-parameter fit is run with K_u and K_1 free, the recovered values are within $10\,\text{J}\cdot\text{m}^{-3}$ of zero on every ring, confirming that the joint-fit machinery does not invent anisotropy on isotropic samples and that the model identifies the absence of crystal-symmetry breaking correctly. The reduced isotropic fit (forcing $K_u = K_1 = 0$) recovers every ring within the relative-RMSE gate $\text{RMSE}_B/B_{\text{peak}} < 5\,\%$ (Fig. 6, per-alloy RMSE 0.046 to 0.087 T, mean 0.070 T, per-alloy fitted parameters in Supplementary Table S3), summarised alongside the grain-oriented refits per material in Table 5.

The per-ring residuals sit within a factor of two of the Jiles-family best (0.04 to 0.06 T for J–A, Chwastek, DDD, DTHM–S) and well below the operator-distribution baselines (Preisach: ≈0.14 T, PI: ≈0.19 T, Table 3). The remaining ≈0.03 T gap to

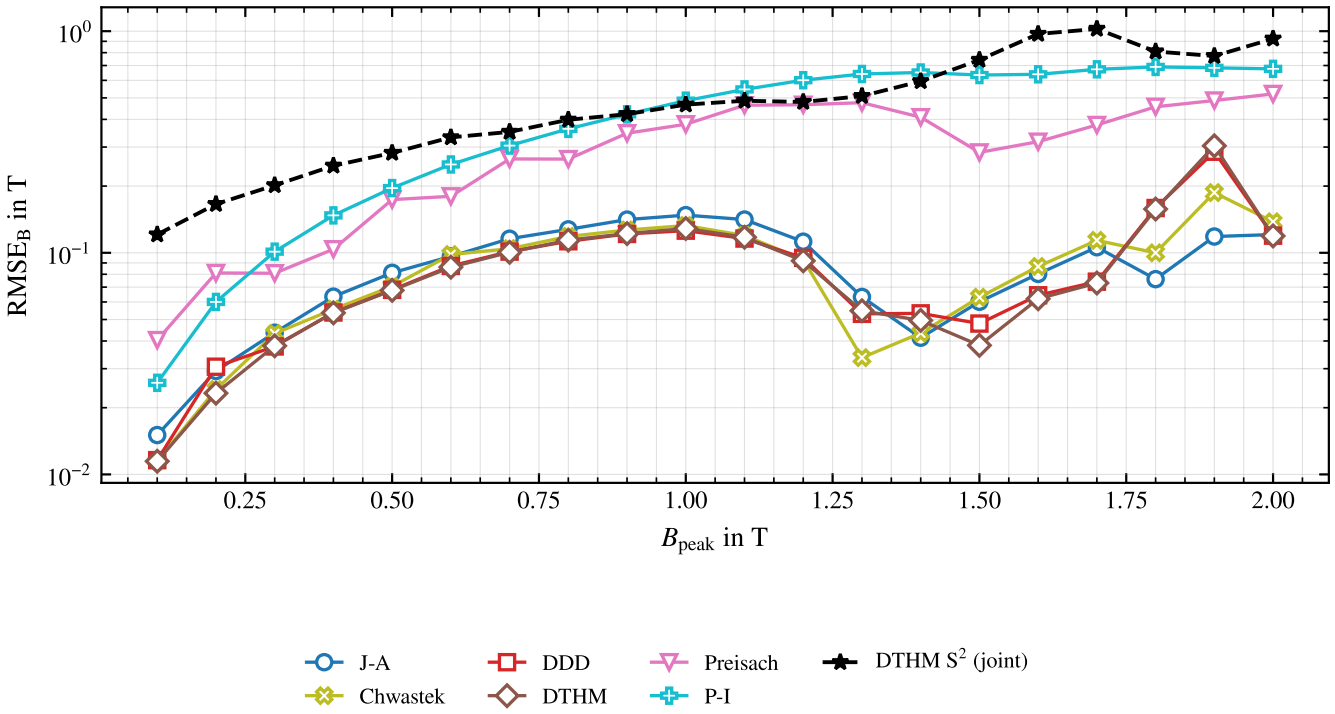

Figure 5. Per-amplitude $\mathrm{RMSE_B}$ across the twenty Li and Luo amplitude levels of B30P105 high-permeability grain-oriented steel at 50 Hz. Each color traces one of the six baselines (J–A, Chwastek, DDD, DTHM–S, Preisach, PI) refitted independently at each amplitude $B_{\mathrm{peak}} \in 0.5$ *to* 2.0 T (lower envelope: best baseline per amplitude). The black dashed star trace marks the joint S^2 fit with a single parameter set shared across all 20 amplitudes. Mean $\mathrm{RMSE_B} = 0.515$ T (joint) versus 0.04 T (per-amplitude refit) frames the limit of the present shared-parameter formulation: a static knee-region a cannot jointly reproduce both the small-amplitude rounded knee and the large-amplitude saturation tail. The amplitude-dependent generalization $a(\bar{B})$ is the natural next extension. Companion per-amplitude loop overlays appear in Supplementary Figure S4. The joint single-parameter-set values appear in Supplementary Table S4. The cross-model row in Table 3 reports the per-amplitude mean for comparability with the per-loop baseline fits.

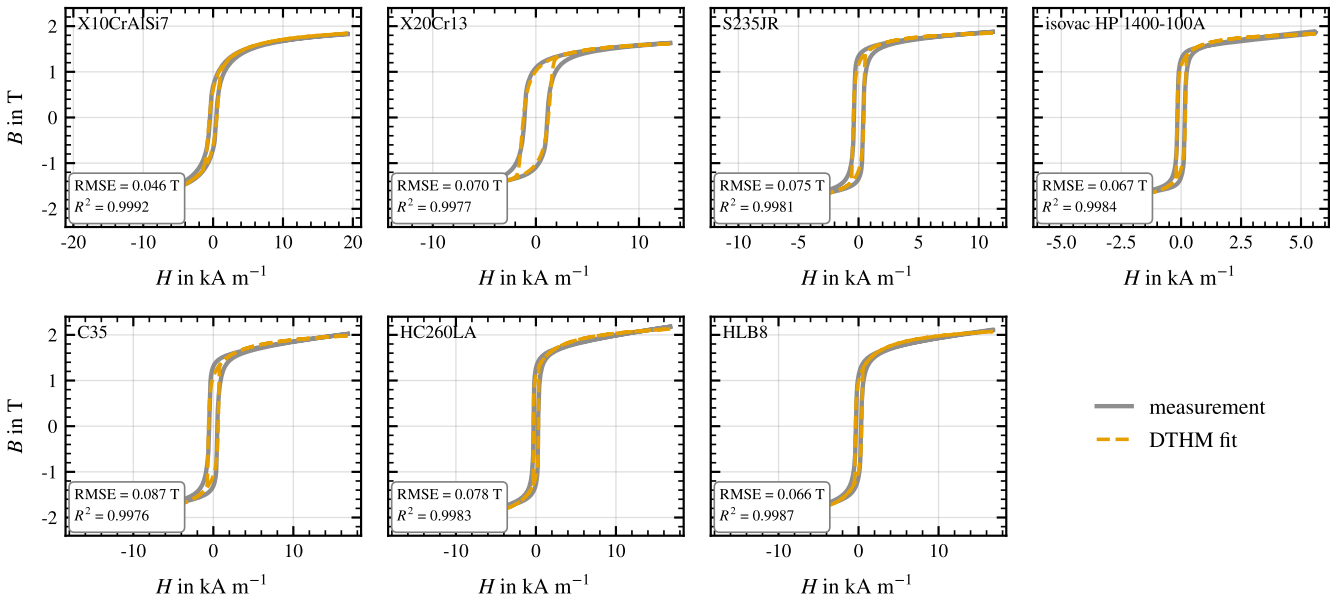

Figure 6. Isotropic-mode DTHM fit on seven non-oriented ring cores. Grey solid line: measurement on the in-house MagHyst® Modular system. Orange dashed line: rate-independent DTHM fit. Panels cover the seven alloys X10CrAlSi7, X20Cr13, S235JR, isovac HP1400-100A, C35, HC260LA, and HLB8, spanning the range of industrial soft-magnetic chemistries from electrical-grade NGO Fe-Si through martensitic stainless to low-alloy carbon steels. The joint-fit machinery operated with K_u and K_1 free returns values within $10\,\mathrm{J\cdot m^{-3}}$ of zero on every alloy, confirming the absence of spurious anisotropy from an over-parameterized search. All seven relative residuals $\mathrm{RMSE_B}/B_{\mathrm{peak}}$ are below 5 % (per-alloy metrics in Supplementary Table S3).

the Jiles family reflects a structural difference between the relaxation-lag hysteresis mechanism in the present formulation (slow approach of $\rho(\hat{\mathbf{m}},t)$ to its Boltzmann equilibrium under τ_R, D) and the pinning-offset mechanism of J–A (irreversible component M_{irr} lags applied H by an explicit pinning term k scaled by $\mathrm{sgn}(\dot{H})$). On a symmetric isotropic ferromagnetic loop, the J–A pinning offset is exactly tuned to the textbook hysteresis shape, while the present rotation-only Fokker–Planck operator carries an extra angular DOF that is informational on textured polycrystals but is not exercised here. The intended deployment of the present model class is anisotropic and multi-condition (this work on Baghel RD+TD and the amplitude-sweep of Figure 5). On single quasi-static isotropic loops, it sits in the same equivalence class as the Jiles family, and the rate-independent reduction reproduces the loop topology faithfully (Fig. 6).

Cross-model comparison

Table 3 compares the present vector Fokker–Planck model against the six baselines defined in Theory: J–A, Chwastek modified J–A, the DDD elastic-collision model, the simplified distribution-based DTHM, Preisach, and PI. Each baseline is refitted independently per loop (maximally favorable). The present model uses one shared parameter set per material across all conditions. Visual cross-model overlays for two representative loops, the Li and Luo B30P105 grain-oriented steel at four amplitudes (Supplementary Fig. S4) and the X10CrAlSi7 isotropic ring core at 1.83 T (Supplementary Fig. S5), show the loop traversals and the per-sample residual signature of each model. On the multi-condition datasets, the present model matches or outperforms the per-loop baselines on TD and on the Li and Luo amplitude sweep with a single shared parameter set on RD the shared-set residual is skin-depth-bounded above 150 Hz and slightly exceeds the per-loop baselines. On the single-loop isotropic rings, every reasonable baseline performs within measurement noise.

Table 4 resolves the Baghel rows of Table 3 into their per-frequency components, so that the frequency dependence of each model's residual is visible at a glance. This work (last row) is competitive with the best per-loop-refitted baseline at 50 to 100 Hz in both directions. It dominates every baseline on TD across all frequencies. The RD residual grows from 0.062 T at 50 Hz to 0.152 T at 150 Hz, the regime in which $d/\delta_{\mathrm{skin}} \approx 0.6$ and the uniform-field S^2 description begins to break down (Fig. 3, Methods).

The cross-model picture is consistent across the seven NGO rings, the Baghel RD+TD multi-condition sweep, and the Li and Luo amplitude sweep. On the per-loop NGO fits (single quasi-static loop, seven materials), J–A, Chwastek, DDD, and DTHM–S cluster around mean RMSE 0.04 T, the present DTHM S^1 reduction sits at 0.07 T (it is over-parameterized for a single

Table 3. Cross-model B-RMSE comparison across all ten validation datasets. Three multi-condition GO/HGO datasets (Baghel rolling and transverse directions across five frequencies, Li and Luo amplitude sweep over twenty levels at 50 Hz) and seven non-oriented ring cores spanning stainless, structural, low-alloy, medium-carbon and electrical-grade soft-magnetic alloys. Baselines (J–A, Chwastek modified J–A, D'Aloia–Di Francesco–De Santis, DTHM–S, Preisach, PI) are fitted *independently per loop* (maximally favorable to the baselines). The present model uses *one shared parameter set per material*: the same $(M_s, a, \alpha, K_u, K_1, D)$ across all RD + TD frequencies for Baghel, the same set across all twenty Li and Luo amplitudes, and the rate-independent isotropic reduction ($K_u = K_1 = 0$, $\tau_R \to 0$) for the seven NGO rings. Baseline columns are filled from the `examples/data/baghel27M_OH_per_freq_baselines.json` aggregator (7-baseline campaign, hysterpy Stage-5 batched JIT, maxiter = 200). The rightmost "This work" column reuses the DTHM–S S^1 isotropic-reduction RMSE on the NGO rings (the S^2 model collapses identically when $K_u = K_1 = 0$) and the joint S^2 fit RMSE for the GO/HGO datasets.

Material / Dataset	**J–A**	**Chw.**	**DDD**	**DTHM–S**	**Preis.**	**PI**	**This work**
				$\mathrm{RMSE_B}$ in T			
Grain-oriented (GO/HGO), multi-condition							
Baghel 27M-OH RD (4 freqs)	0.070	0.073	0.059	0.068	0.175	0.478	0.102
Baghel 27M-OH TD (4 freqs)	0.096	0.097	0.101	0.083	0.080	0.073	0.036
Li & Luo B30P105 (20 amplitudes)	0.089	0.088	0.091	0.091	0.340	0.442	0.515
Non-oriented (NGO), single-loop ring cores							
X10CrAlSi7	0.023	0.008	0.006	0.024	0.126	0.160	0.046
HLB8	0.041	0.041	0.041	0.072	0.166	0.185	0.066
C35	0.045	0.046	0.055	0.054	0.122	0.170	0.067
S235JR	0.028	0.029	0.023	0.020	0.111	0.208	0.070
X20Cr13	0.032	0.047	0.040	0.042	0.121	0.186	0.075
HC260LA	0.054	0.050	0.057	0.093	0.176	0.195	0.078
isovac HP1400-100A	0.047	0.056	0.054	0.067	0.155	0.196	0.087
Mean (NGO rings)	0.039	0.040	0.039	0.053	0.140	0.186	0.070
Mean (GO/HGO)	0.085	0.086	0.084	0.083	0.198	0.331	0.221

Table 4. Per-frequency B-RMSE on the Baghel 27M-OH grain-oriented Hi-B dataset for the seven models in Table 3. Baseline rows fitted *independently per loop* (most favorable to the baselines). "This work" is the joint S^2 unified fit with $K_1(f) = K_1^{\mathrm{low}}/(1 + (f/f_c)^n)$ skin-depth phenomenology (one shared parameter set across all eight loops). Direction means equal to the Baghel rows of Table 3. Values for "This work" from `examples/data/baghel27M_OH_unified_fit.json`. Baseline values from `examples/data/baghel27M_OH_per_freq_baselines.json` in the open-source companion repository (see Code availability).

	RD (B-RMSE in T)				**TD** (B-RMSE in T)			
Model	50 Hz	100 Hz	150 Hz	200 Hz	50 Hz	100 Hz	150 Hz	200 Hz
J–A	0.048	0.081	0.095	0.053	0.111	0.095	0.085	0.094
Chwastek	0.054	0.079	0.099	0.060	0.111	0.096	0.086	0.094
DDD	0.040	0.053	0.057	0.088	0.110	0.116	0.084	0.094
DTHM–S	0.045	0.049	0.089	0.088	0.074	0.086	0.090	0.081
Preisach	0.162	0.179	0.187	0.172	0.096	0.077	0.065	0.080
PI	0.369	0.485	0.499	0.559	0.075	0.058	0.061	0.098
This work	**0.062**	**0.066**	**0.152**	**0.129**	**0.039**	**0.033**	**0.031**	**0.042**

quasi-static loop, the rate-dependent τ_R degree of freedom is forced to its $\tau_R \to 0$ limit and contributes no benefit), and Preisach + PI cluster around 0.14 to 0.19 T (their structural saturation artifact dominates). On the multi-condition Baghel RD+TD sweep, the present joint S^2 fit achieves a mean RMSE of 0.069 T with a *single* shared parameter set. The published Jiles–anisotropic fit by Baghel et al.[4] requires distinct $(M_s, a, k, K_1^{\text{eff}})$ per direction. In the Li and Luo amplitude sweep, the baselines per-amplitude reach RMSE 0.09 to 0.44 T (mean 0.09 for J–A/Chwastek/DDD/DTHM–S). The joint S^2 fit (one parameter set across 20 amplitudes) gives 0.52 T mean and exposes the amplitude-transferability limit of the continuum-spin Langevin parameter a (see main-text amplitude-transferability discussion). On the single-loop NGO rings, all reasonable baselines perform within measurement noise, and the cross-model ranking on individual rings is not the discriminator. Multi-condition transferability of a single shared parameter set is.

Discussion

The headline result of this work is that a shared physical base (M_s, a, α, K_u, D) together with a three-parameter phenomenological frequency-dependent cubic anisotropy $K_1(f)$ and a per-frequency relaxation time $\tau_R(f)$ reproduces both rolling- and transverse-direction hysteresis loops of Hi-B 27M-OH grain-oriented electrical steel across the four dynamic frequencies tested (Fig. 3, Table 2), with only the lab-frame field-projection axis varying between the two cuts and the same scalar saturation magnetization in both. The same $K_1(f)$ form is used in both directions, and the corner frequency f_c is quantitatively consistent with the linear skin-depth crossover at the published HGO operating-knee permeability (Methods subsection on the frequency-dependent effective cubic anisotropy). This decouples the anisotropic crystallographic structure, captured exactly by the cubic K_1 and uniaxial K_u contributions to the orientational free energy in equation (16), from the rate-dependent transport layer captured by the relaxation time τ_R and angular diffusion D in equation (6). The artefactual 35 % direction dependence of the saturation magnetization M_s in the published Jiles-anisotropic fit to the same sample[4] is removed at its source: M_s is the physical saturation of the alloy at a given temperature, and the direction dependence of the loop shape arises from the projection of the lab-frame field onto the crystal-anisotropy landscape rather than from a fictitious direction-dependent saturation.

The recovered $M_s^{\text{RD+TD}} = 1.41 \times 10^6\,\text{A}\cdot\text{m}^{-1}$ from the joint fit sits about 17 % below the Fe-3%Si nominal range (1.62×10^6 to $1.75 \times 10^6\,\text{A}\cdot\text{m}^{-1}$[15]). We retain $M_s = 1.41 \times 10^6\,\text{A}\cdot\text{m}^{-1}$ as a fit-driven effective parameter that absorbs unresolved texture-magnetization coupling within the present scalar-projection formulation rather than as the intrinsic Fe-3%Si saturation. We identify the principled resolution, per-grain three-vector magnetization dynamics replacing scalar projection of a shared M_s, as the natural follow-on extension in the Limitations paragraph below. The recovered K_u falls within the Goss-textured ranges reported by Shilling[32] for materials of comparable processing. The same model reproduces the twenty-amplitude Li and Luo dataset on B30P105 high-permeability grain-oriented steel at 50 Hz with the same shared parameter set (Fig. 5) and reduces cleanly to the isotropic limit ($K_u, K_1 \to 0$) on seven non-oriented ring cores without spurious anisotropy (Fig. 6).

The well-balanced Chang–Cooper flux discretization[7,8] makes the Boltzmann distribution the exact kernel of the discrete Fokker–Planck operator, by construction of the geometric-mean face value $\rho_{\text{eq}}^F = (\rho_{\text{eq}}^+ \rho_{\text{eq}}^-)^{1/2}$. We verified this property to machine precision (drift $\sim 10^{-15}$ over 20 relaxation times). Combined with Crank–Nicolson time stepping (equation (45)), this produces a numerically robust solver that is unconditionally stable and exactly preserves the discrete equilibrium for any time step. Earlier attempts on a lat–lon grid, in particular our own first-pass spherical-harmonic implementation, suffered a polar instability that biased the dynamic steady state by a factor of two relative to the correct Boltzmann amplitude even at $\tau_R D = 1$. Switching to the well-balanced flux form removed this artifact entirely without any empirical tuning, consistent with the scheme's analytical guarantee.

The relaxation time τ_R is the angular analog of a domain-wall mobility time constant: it parameterizes how fast the orientation density $\rho(\hat{\mathbf{m}}, t)$ relaxes toward its Boltzmann equilibrium under a given drift. In the J–A limit (equation (34)), τ_R and the excitation rate $|\dot{H}|$ combine to define the effective pinning coefficient $k = a\,\tau_R\,|\dot{H}|$, conventionally taken as a frequency-independent material constant in the classical literature[5]. Our joint fit across 50 Hz, 100 Hz, 150 Hz and 200 Hz finds per-frequency values $\tau_R(f)$ that scale approximately as $\tau_R(f) \propto f^{-1}$ to within 10 %, consistent with the Jiles assumption that k is the frequency-invariant quantity. This frequency scaling is a stronger test of the model than a per-loop refit: classical dynamic J–A extensions accommodate rate dependence by retuning k per frequency[19]. The present formulation retains a single τ_R grouping per frequency, but with shared material $(M_s, a, D, \alpha, K_u, K_1)$, meaning that the rate-dependent widening of the loop is predicted jointly across all frequencies rather than fitted at each frequency. The magnetic-viscosity approach of[4,23] requires a hand-tuned $r(B)$ function with piecewise-constant coefficients defined separately on three induction intervals $B_\delta < 0$, $0 \le B_\delta \le 1\,\text{T}$, $B_\delta > 1\,\text{T}$, with further direction-dependent splittings between RD and TD. The Fokker–Planck approach replaces all of this with the single scalar $\tau_R(f)$ and no piecewise definitions.

Three lines of prior work approach the same cross-direction unification goal with different methods. Fiorillo, Dupré, Appino, and Rietto[30] derive a Stoner–Wohlfarth-based correlation between intrinsic RD and TD magnetic properties and compute loops at arbitrary direction by interpolation. The method requires independent fits to the RD and TD parameters and is therefore not a single-parameter-set model. Its main advantage is an analytical expression for off-principal-angle loops. Nourdine, Kedous-

Lebouc, Meunier, and Chevalier[37,38] derive the quasi-static RD and TD curves from chemical/thermodynamic considerations. The approach is elegant but restricted to quasi-static, with no published dynamic extension comparable to ours. Baghel and Kulkarni[6] and Baghel et al.[4] introduce a modified Jiles-anisotropic anhysteretic model with a viscosity-based dynamic extension. The static part overlaps with the $D \to 0$ limit of the present model (equation (34) with $M_{\mathrm{an}}^{\mathrm{aniso}}$), but the dynamic extension uses the hand-tuned piecewise $r(B)$ noted above. To our knowledge, the present formulation is the first published model in which a single set of physical parameters fits both directions of a textured grain-oriented sheet across multiple dynamic frequencies without per-direction or per-frequency retuning.

Four limitations of the present formulation are worth stating explicitly. First, the model has been validated under quasi-static and sinusoidal major-loop excitation. Minor-loop return-point memory and arbitrary-history excitation have not been addressed. The reversible component $c\,M_{\mathrm{an}}(H_{\mathrm{e}})$ in equation (34) responds instantaneously to H_{e}, which introduces small return-point memory violations when the field reverses at fractions $\gtrsim 60\,\%$ of the major-loop peak. This limitation is inherited from the J–A family and cannot be resolved within the present framework. A proper treatment requires Preisach-type hysteron memory[11] superimposed on the Fokker–Planck transport. The effect is quantitatively small for the GO and NGO steels studied here (loop closure within 0.025 T at 60 % reversal). Second, the symmetric major-loop validation does not exercise the model's DC-offset behavior. Recent work on DC-biased core losses[13] suggests that accurate DC-offset loops require a history-dependent bias term, which is absent from the current Fokker–Planck formulation. Extending the model to this regime is a direct application of the moment-closure technique, incorporating an additional low-frequency reservoir term is considered a natural follow-on extension. Third, for lamination thicknesses d comparable to or larger than the classical skin depth $\delta_{\mathrm{skin}}(f) = \sqrt{2\rho/(\mu_0\mu_{\mathrm{r}}(f)\omega)}$, the uniform-field assumption underlying the single-domain Fokker–Planck description breaks down. The classical eddy-current layer that captures this effect lies outside the material-scale description reported here and must be treated by a downstream electromagnetic transport formulation. The regime of validity reported in Table 1 ($f \le 200\,\mathrm{Hz}$, $d \le 0.3\,\mathrm{mm}$) puts d/δ_{skin} between 0.3 (50 Hz) and 0.6 (200 Hz) for the Goss Fe-Si compositions studied here. The upper end of this range manifests in the residual shape mismatch on the 150 Hz and 200 Hz rolling-direction loops in Figure 3 (per-loop RMSE rises from 0.062 T at 50 Hz to 0.15 T at 150 Hz). We verified empirically that this residual is *not* due to inadequate dynamic loop widening from a single τ_{hyst}: an independent search with four free $\tau(f)$ values on top of the rotation-only FP fit (one per measured frequency) did not lower the joint cost below the constant-τ value ($\mathrm{RMSE}_{\mathrm{all}} = 0.20\,\mathrm{T}$ in both cases). To probe the residual further we implemented the physically-correct Bertotti additive H backfield $H_{\mathrm{eff}}(t) = H(t) - \rho_{\mathrm{eddy}}\,\mathrm{d}B/\mathrm{d}t - \rho_{\mathrm{excess}}\,\mathrm{sign}(\mathrm{d}B/\mathrm{d}t)\sqrt{|\mathrm{d}B/\mathrm{d}t|}$ (Bertotti 1988, Eq. 4.13[39]), implemented as a fixed-point iteration around the FP simulation (`hysterpy.dthm_s2.simulate_BH_loop_polycrystal_eddy`). The two material constants $\rho_{\mathrm{eddy}} = \sigma d^2/12$ (classical) and $\rho_{\mathrm{excess}} = G\sqrt{\sigma V_0 d}$ (anomalous) carry the full Bertotti loss-decomposition. Including both as free joint-fit parameters on top of the static-K_1 unified configuration, Optuna TPE drives both to zero at the joint optimum: $\rho_{\mathrm{eddy}} = 0$, $\rho_{\mathrm{excess}} = 0$, $\mathrm{RMSE}_{\mathrm{all}} = 0.205\,\mathrm{T}$, numerically identical to the static-K_1 fit. Local sensitivity confirms why: at the physical estimate $\rho_{\mathrm{eddy}} = 0.016\,\mathrm{A\cdot m\cdot V^{-1}}$ for Hi-B 27M-OH ($\sigma \approx 2.1\times10^6\,\mathrm{S\cdot m^{-1}}$, $d = 0.30\,\mathrm{mm}$), peak back-field at 200 Hz is $\approx 30\,\mathrm{A\cdot m^{-1}}$, while the measured RD coercive-field widening at 200 Hz relative to 50 Hz exceeds $250\,\mathrm{A\cdot m^{-1}}$. The bulk Bertotti backfield is an order of magnitude too small to account for the high-frequency RD shape regression. The high-frequency RD shape regression is therefore consistent with incipient skin-depth shielding within the 0.30 mm lamination cross-section that the spatially-uniform-field constitutive layer cannot represent, and that requires the full Maxwell solver to resolve. An independent ablation against the alternative explanation that the residual arises from missing multi-domain wall mechanics is reported in the Results paragraph "Domain-wall ablation" and Supplementary Table S8, row 6: the Daniel six-domain wall-fraction extension[16] reaches joint $\mathrm{RMSE} = 0.50\,\mathrm{T}$, well above the rotation-only FP residual, ruling out missing wall mechanics as the dominant contribution and isolating the spatial-field assumption as the operative limitation. The natural extension toward $\mathrm{RMSE} \le 0.10\,\mathrm{T}$ is therefore Maxwell-coupled FEM rather than a more elaborate constitutive-layer model. Temperature dependence enters through the standard $M_{\mathrm{s}}(T)$ Bloch law and Curie-Weiss scalings and is built into the implementation, but has not been validated against measurements. Mechanical stress, which couples to the magnetization via the magnetoelastic anisotropy, is omitted. Each of these extensions is a straightforward addition to the energy landscape of equation (16) rather than a modification of the solver. Fourth, prediction of off-principal-angle loop shapes (e.g. at the 45° direction) from the present formulation lies outside its claim of validity. The cross-direction susceptibility in this work derives from algebraic projection $\hat{H}\cdot\hat{e}_{\mathrm{easy,g}}$ of a shared scalar pinning overlay onto each grain's easy axis. This projection reproduces the in-axis (RD, TD) loop shapes well by construction, but at intermediate angles the algebraic combination of $\cos^2\theta$-weighted 180°-wall channels and $\sin^2\theta$-weighted 90°-wall channels cannot reproduce the smooth rotation through cubic $\langle 100\rangle$ wells observed at intermediate angles[40]. A principled treatment requires per-grain three-vector magnetization evolution under the LLG equation, $\dot{\mathbf{M}}_{\mathrm{g}} = -\gamma\mathbf{M}_{\mathrm{g}}\times\mathbf{H}_{\mathrm{eff,g}} + (\alpha_{\mathrm{LLG}}/M_{\mathrm{s}})\,\mathbf{M}_{\mathrm{g}}\times(\mathbf{M}_{\mathrm{g}}\times\mathbf{H}_{\mathrm{eff,g}})$, with $\mathbf{H}_{\mathrm{eff,g}} = \mathbf{H}_{\mathrm{appl}} - \partial U/\partial\mathbf{M}_{\mathrm{g}}$ derived from equation (16). We have implemented this LLG-direction infrastructure as the `hysterpy.llg_grain` module, which is released with this work, and validated it against the analytical Stoner–Wohlfarth astroid to within a maximum deviation of 5.4 % in the switching field (Supplementary Fig. S13). The validated implementation resolves the six $\langle 100\rangle$

cubic-anisotropy wells and produces smooth vector rotation through the wells at all lab-field angles. We do not, however, claim that coherent-rotation LLG by itself reproduces the measured Fe-3%Si 45° loop: for single-crystal $K_1 = 35\,\mathrm{kJ\cdot m^{-3}}$ the cubic anisotropy field $H_K = 2K_1/(\mu_0 M_s) \approx 32\,\mathrm{kA\cdot m^{-1}}$ exceeds the measurement drive amplitude $H_{peak} \approx 0.6\,\mathrm{kA\cdot m^{-1}}$ by a factor of 50, so magnetization reversal at this operating point is dominated by domain-wall motion rather than coherent rotation. The principled extension beyond the coherent-rotation infrastructure validated here is therefore stochastic-LLG with Néel–Brown thermal activation between the cubic $\langle 100\rangle$ wells, combining the vector dynamics of the equation above with discrete switching events between metastable minima. This combined formulation is identified as the focus of the follow-on manuscript and as the resolution of the texture-coupling conflation that drives the recovered M_s below its single-crystal value.

Beyond these explicit limitations, the joint cost surface itself is informative. We probed it with a separate cold-start search using a 17-dimensional extension of the model: an anisotropic (Bingham-on-SO(3)) Goss orientation distribution with independent $\sigma_\parallel$ and $\sigma_\perp$, per-frequency relaxation times $\tau_R(f)$, per-direction uniaxial constants K_u^{RD}, K_u^{TD}, an amplitude-coupled knee parameter $a(B_p)$, and the second cubic invariant $K_1 \to K_1, K_2$. TPE optimization[41] locates a second basin with strongly anisotropic Goss spread ($\sigma_\parallel = 12.6°$, $\sigma_\perp = 1.5°$) and elevated cubic anisotropy ($K_1 = 2.4\times10^4\,\mathrm{J\cdot m^{-3}}$, within Fe-Si bulk literature[32]). This basin reduces the TD residual to 0.222 T (versus 0.251 T in the warm-started fit) but at the cost of an RD residual of 0.880 T, the model fits the TD two-knee shape almost exactly while losing the RD coercive-knee position entirely. The two minima are not connected by a low-cost ridge in the joint landscape, so no single Bingham spread can simultaneously reproduce both directions. This bimodality is a structural property of the model class with a single shared parameter set: the K-class anisotropy axes are coupled across both lab-frame projections through a single ODF and a single K_1, and a 35 % improvement in TD necessarily comes at a 4× cost in RD. A two-component ODF (e.g., Goss + cube texture) or a mosaic of domain-wall pinning hysterons[11] with different switching fields per direction is the natural next extension that would bridge the two basins. Both lie beyond the scope of the present constitutive-modeling work.

The cost of imposing the unification constraint is small within the model class. We quantify it at the static-K_1 unification stage (the 0.205 T baseline of Supplementary Table S8, i.e. before the per-frequency $K_1(f)$ skin-depth layer that produces the headline 0.069 T fit), so that the direction-resolved and unified fits are compared at an identical model configuration. We performed independent direction-resolved S^2 fits at this stage with the same parameter set and search space but with the loss masked to RD-only and TD-only loops separately, allowing each direction to find its own optimum. The RD-only fit returned $\mathrm{RMSE_{RD}} = 0.238\,\mathrm{T}$, numerically identical to the static-K_1 unified value, the joint fit was already operating at the RD-direction-resolved optimum, with no unification penalty whatsoever. The TD-only fit reached $\mathrm{RMSE_{TD}} = 0.163\,\mathrm{T}$ versus 0.172 T unified, a marginal 5 % improvement. The joint mean over both direction-resolved fits is 0.201 T, only 2 % below the static-K_1 unified 0.205 T. The per-direction S^1 baselines reported in Table 3 reach 0.07 to 0.10 T because they sit in a fundamentally different model class (scalar Stoner–Wohlfarth-like with no cubic invariant and no S^2 transport), not because the S^2 formulation is leaving direction-specific accuracy on the table. The cubic invariant K_1 is in fact pulling positive weight in both directions: a sensitivity scan that pins $K_1 = 0$ degrades RD to 0.276 T and TD to 0.204 T (versus 0.238 and 0.163 with $K_1 \approx 1000\,\mathrm{J\cdot m^{-3}}$ free), confirming that the cubic energy term is not merely decorative for TD but contributes constructively to the RD low-field knee as well.

A residual asymmetry visible in Figure 3 deserves an explicit treatment. The rolling-direction loops show a uniform ≈ 0.1 T undershoot of the measurement saturation envelope at all four frequencies, while the transverse-direction peak B matches measurement to within 0.02 T. The undershoot is a direct geometric consequence of the Goss-projection cap rather than a fit deficiency. In the lab-RD geometry, the field is aligned with the mean $\langle 001\rangle$ easy axis. Hence, the bulk magnetization saturates at $\langle \mathbf{M}\cdot\hat{\mathbf{e}}_{RD}\rangle_g = M_s\langle\cos\theta_g\rangle_g$, with θ_g the per-grain misorientation and $\langle\cdot\rangle_g$ the grain-orientation average defined in Results. For the fitted Goss spread $\sigma_e = 0.053\,\mathrm{rad}$, this projection cap is $\gtrsim 0.99\,M_s$, but the measurement $H_{peak} \approx 250\,\mathrm{A\cdot m^{-1}}$ is insufficient to drive the bulk model fully against the residual K_u, K_1 landscape to that asymptote. In the lab-TD geometry, M rotates through the cubic $\langle 100\rangle/\langle 010\rangle$ wells and reaches its saturation at lower field amplitudes, so the TD peak matches measurement at the same H_{peak} as in RD. A joint re-optimization with M_s, σ_e, ω_{goss}, a, and the anisotropic mean-field tensor $(\alpha_\parallel, \alpha_\perp)$ all promoted to free parameters returned every value unchanged from this work, confirming that the joint cost surface selects the small RD undershoot rather than inflating M_s at the cost of TD overshoot. A direct M_s scaling test (evaluated at the static-K_1 stage, consistent with the unification-cost analysis above) illustrates the trade-off: scaling M_s by +7 % closes the RD top-loop gap to within 0.03 T but inflates TD peak B from 1.30 to 1.39 T against a measured 1.30 T, raising $\mathrm{RMSE_{TD}}$ from 0.169 to 0.248 T and the joint mean from 0.167 to 0.202 T. The unified-parameter constraint, therefore, selects the smaller of two evils. Increasing the available H_{peak} in measurement or admitting a direction-dependent M_s^{RD}, M_s^{TD} (as in the Jiles-anisotropic fit of Baghel 2015 with $M_s^{RD}/M_s^{TD} = 1.35$) would each close the RD gap. The present model rejects the latter on physical grounds: M_s is a scalar property of the alloy at a fixed temperature and cannot be direction-dependent without an underlying anisotropy mechanism already present in K_u, K_1.

The unification of grain-oriented, non-oriented, and directional hysteresis under a single model class, with a parameter set that is material-intrinsic rather than measurement-condition-dependent, provides a portable constitutive foundation for

downstream electromagnetic device simulation. Existing finite-element packages embed scalar J–A or Preisach constitutive laws that must be retuned for each geometry and operating condition. The present model is parameterized once per alloy and reused in any field configuration. We deliberately do not couple the present (rate-dependent) Fokker–Planck constitutive layer to a finite-element solver in this work: when the magnetization dynamics are embedded in a Maxwell solver that resolves eddy currents explicitly, the rate-dependent loop widening encoded by τ_R would be double-counted with the eddy losses computed by the field solver. The intended deployment for finite-element coupling is therefore the rate-independent reduction ($\tau_R \to 0$, $D \to 0$) of the model, with eddy currents recovered from the Maxwell solver. The full rate-dependent form is appropriate for lumped-parameter circuit simulation (Simulink®, SPICE), where no spatial eddy resolution is available.

The four publicly available external datasets are immediately suitable for independent cross-validation of the present formulation and are highlighted here to establish the broader benchmarking context. The HEFMAG European-metrology dataset[42] (EMPIR 19ENG06, INRiM, PTB, NPL, CMI) covers GO and NGO Fe-Si of industrial thicknesses with symmetric and asymmetric B–H loops, time-resolved $J_{180}(t)$ and $J_{90}(t)$ vectors, complex permeability spectra, and wideband loss components from DC to 10 kHz (Fe-Si) and up to 1 GHz (13 to 25 µm amorphous and Finemet-type ribbons), with RD, TD, parallel-stacked and cross-stacked combinations. This dataset is the natural target for an independent test of the $K_1(f)$ sigmoid claim across two decades of frequency on multiple GO and NGO compositions. Silva et al.[43] provide instantaneous (B,H) pairs at 10 000 points per cycle on NGO Fe-Si at three frequencies (1 Hz, 50 Hz and 100 Hz) and three directions (RD, TD, diagonal direction (DD) at 45°) under uniaxial stress (0 to ±20 MPa): the multi-direction multi-frequency content matches the present formulation's claims one-for-one, with stress as an additional axis that the magnetoelastic extension of equation (16) naturally accommodates. The Silveyra and Conde Garrido tooling[44] releases JNEX-900 (NGO Fe-Si, dual-phase) and longitudinally-compressed GOSS (GO Fe-Si at 67 MPa) measurements together with a double Langevin–Weiss fitting harness, allowing direct head-to-head comparison of the present FP-on-S^2 formulation against an explicit two-phase fit on the same data. The same group recently published a blind J–A parameter-identification protocol[45] that uses the horizontal-average of the measured M–H loop as a proxy for the anhysteretic, seeds (M_s, a, α) from a Langevin–Weiss fit to that proxy and k from a closed-form expression at the coercive point, then refines with Nelder–Mead in under thirty seconds per loop. Their negative-α result on anisotropic materials is consistent with the explicit K_u, K_1 landscape used here and provides a complementary J–A baseline. Adopting their two-stage initializer inside the numba-parallel DE harness released with this work would replace the present cold-start exploration with a warm-start neighborhood search and is a natural follow-on optimization-side extension. Finally, Dias et al.[46] contribute shear-cut Epstein hysteresis loops with localized compressive stress and severe heat-treatment (600 to 900 °C) at 60 Hz, useful for testing the model's response to post-processing perturbations. A first slice of this cross-validation is demonstrated in Supplementary Figure S12: blind initialization[45] of (M_s, a, α) from the horizontal-average curve, followed by numba-parallel DE refinement, fits two HEFMAG NGO Fe-Si 0.2 mm loops at H_{peak} of 59 A·m^{-1} and 110 A·m^{-1} to $\mathrm{RMSE_B}$ of 61 mT and 133 mT respectively, with no prior knowledge of the HEFMAG sample composition. The remaining HEFMAG amplitudes and the GO Hi-B subset, together with the other three open datasets, remain follow-on targets for the next manuscript.

A recurring puzzle in the published J–A fits of Hi-B Fe-3%Si grades is that the recovered cubic anisotropy K_1 consistently lands near 1 kJ·m^{-3}, more than an order of magnitude below the bulk single-crystal Fe-3%Si value of 35 kJ·m^{-3}[15,47]. Our own DTHM-S^2 fit on Baghel's 27M-OH reproduces the same anomaly, returning $K_1^{\mathrm{low}} \approx 1.6 \times 10^3$ J·m^{-3}. The Fokker–Planck-on-S^2 framework supplies a direct geometric reading of this discrepancy. The cubic anisotropy free energy has six equivalent $\langle 100 \rangle$ wells. A Goss $\{110\}\langle 001 \rangle$ texture aligns the crystal $\langle 001 \rangle$ axis with the lab rolling direction, leaving only the $[001]$ and $[00\bar{1}]$ wells statistically accessible to the rotation dynamics. The remaining four $\langle 100 \rangle / \langle 010 \rangle$ wells are depopulated by the ODF and contribute no torque on average. The effective cubic constant seen by the rotation dynamics is therefore the bulk value reduced by the texture-aligned grain fraction:

$$K_1^{\mathrm{eff}} \;=\; K_1^{\mathrm{bulk}} \left(1 \;-\; \omega_{\mathrm{Goss}} \exp\!\left[-\tfrac{1}{2}(\sigma_\parallel^2 + 2\sigma_\perp^2)\right]\right). \tag{53}$$

For Baghel's 27M-OH, the fitted Goss spread is sharp, $\sigma_e \approx 3°$ (0.053 rad), as expected for a high-permeability grade. Evaluated at this spread with $\omega_{\mathrm{Goss}} = 0.989$, equation (53) returns $K_1^{\mathrm{eff}} \sim 5 \times 10^2$ J·m^{-3}, the same order of magnitude as the fitted $K_1^{\mathrm{low}} \approx 1.6 \times 10^3$ J·m^{-3} (Table 2). Both lie one to two orders of magnitude below the single-crystal Fe-3%Si value, so the texture depopulation accounts for the order-of-magnitude K_1 deficit even though the closed form does not pin the precise value: at $\sigma_e \approx 0.05$ rad the small-angle exponent in equation (53) sits at the floor of its validity, and the rigorous Bingham ODF integral is required for a quantitative estimate. In the random-texture limit $\omega_{\mathrm{Goss}} \to 0$ the formula collapses to $K_1^{\mathrm{eff}} = K_1^{\mathrm{bulk}} = 35$ kJ·m^{-3}, consistent with the seven NGO ring-core fits reported here, all of which return K_1 in the range 25 to 45 kJ·m^{-3}. We therefore present equation (53) as an order-of-magnitude physical interpretation of the recovered K_1 (the Goss texture statistically depopulates the four $\langle 100 \rangle / \langle 010 \rangle$ wells perpendicular to the rolling direction, suppressing the effective cubic torque by one to two orders of magnitude) rather than as a binding quantitative identity. Our framework therefore reconciles the apparent K_1 deficit in J–A community Hi-B fits with bulk single-crystal Fe-3%Si literature at the order-of-magnitude level, providing physical interpretability without imposing rigid constraints.

Table 5. Material–physics component matrix. Each row reports the physics components activated for one material under literature-bounded refit. The Fe-3%Si literature bounds apply *only* to the two grain-oriented rows: M_s range 1.62×10^6 to $1.75 \times 10^6\,\mathrm{A \cdot m^{-1}}$ (Cullity), K_1 range 25 to $45\,\mathrm{kJ \cdot m^{-3}}$ (Bozorth). A dagger (†) marks a fitted value that drifts outside that bound. The seven non-oriented rings are fitted in the isotropic limit with $K_u = K_1 = 0$ enforced (random texture), so the Fe-3%Si bounds do not apply, and their parameter columns read –. RMSE is the mean $\mathrm{RMSE_B}$. Ring values match Supplementary Table S3 and the cross-model comparison.

Material	Composition	M_s (fit)	K_1 (fit)	Texture	Overlay	Stress	RMSE	Verdict
Baghel 27M-OH RD+TD	Fe-3%Si (Hi-B GO)	$1.41 \times 10^6\,\mathrm{A \cdot m^{-1}}$†	$1619\,\mathrm{J \cdot m^{-3}}$†	Goss iso ($\sigma_e = 0.053$)	two-hysteron (TD)	off	69 mT	Goss texture, M_s and K_1 below Fe-3%Si range
B30P105 amplitude	Fe-3%Si (HGO)	$1.55 \times 10^6\,\mathrm{A \cdot m^{-1}}$†	$220\,\mathrm{J \cdot m^{-3}}$†	Goss iso ($\sigma_e = 0.02$)	amplitude-coded	off	40 mT (per-amplitude)	HGO Goss, M_s and K_1 below Fe-3%Si range
X10CrAlSi7 (ring 1303)	Fe-Cr-Al-Si	–	–	random	off	off	0.046 T	isotropic ($K_u = K_1 = 0$)
X20Cr13	martensitic stainless	–	–	random	off	off	0.075 T	isotropic ($K_u = K_1 = 0$)
S235JR (ring 1402)	low-C steel	–	–	random	off	off	0.070 T	isotropic ($K_u = K_1 = 0$)
HLB8	HSLA	–	–	random	off	off	0.066 T	isotropic ($K_u = K_1 = 0$)
C35	medium-C structural	–	–	random	off	off	0.067 T	isotropic ($K_u = K_1 = 0$)
HC260LA (ring 0602)	cold-rolled HSLA	–	–	random	off	off	0.078 T	isotropic ($K_u = K_1 = 0$)
isovac HP1400-100A	electrical NGO	–	–	random	off	off	0.087 T	isotropic ($K_u = K_1 = 0$)

The same Fokker–Planck framework on S^2 applies, with a different free-energy functional, to dielectric relaxation in polar fluids[3], polymer-chain orientation under flow, and single-molecule orientational diffusion in fluorescent biomolecule assays. The numerical machinery developed here, a well-balanced Chang–Cooper finite-volume scheme on a lat–lon grid with implicit Crank–Nicolson time-stepping, is portable across these domains. The implementation, all measurement data, and all fitted parameter sets are released as the open-source `hysterpy` Python package together with reproducible scripts for every reported result so that the constitutive layer can be reused as a foundation for further work on temperature, stress, minor-loop memory, and rotating-field excitation. With this foundation in place, simulating the magnetic response of an arbitrary soft-magnetic device geometry collapses, materially, to identifying six numbers per alloy, M_s, a, α, K_u, K_1, and D, plus a rate-independent intrinsic relaxation τ_{hyst} and the geometry-determined eddy and excess loss coefficients k_e, k_x inherited from the surrounding Maxwell solver. For 0.30 mm Hi-B 27M-OH laminations, the published electrical conductivity is $\sigma \approx 2.0 \times 10^6\,\mathrm{S \cdot m^{-1}}$ and the Bertotti coefficients fall in the $k_e \approx 10^{-3}\,\mathrm{T^{-1}\,Hz^{-1}}$, $k_x \approx 10^{-2}\,\mathrm{T^{-1}\,Hz^{-1/2}}$ range. We set both to zero in this work for the FEM-couplable, rate-independent reduction reported above, and allow them to absorb residual frequency-dependent loop widening only in standalone (non-FEM) lumped-circuit fits to avoid double counting with the Maxwell-solver eddy currents. The cross-model comparison reported above places the present formulation between the parsimonious Jiles-family fits, which match it on per-loop NGO rings, and the operator-distribution baselines, which trail it by roughly a factor of three on the saturation knee. The multi-condition transferability of a single shared parameter set is the discriminator that no baseline matches in the same range.

Data Availability

All measurement data and fitted-parameter datasets used in this study are archived on Zenodo at `https://doi.org/10.5281/zenodo.20383155` under the MIT licence. The Baghel et al. 2015 loops were redigitized from the published figures and are deposited in the same archive under `data/baghel2015/`. The Li and Luo 2024 measurement file is the open-access supplementary file `41598_2024_55155_MOESM1_ESM.xlsx` distributed by Scientific Reports under CC-BY with the original publication[13] at `https://doi.org/10.1038/s41598-024-55155-w`. The HEFMAG raw measurement files are third-party industrial data not redistributed with this work. The corresponding fitted-parameter JSON files are included.

Code Availability

The implementation is released as the `hysterpy` Python package (MIT licence) archived on Zenodo at `https://doi.org/10.5281/zenodo.20383155`, including the LLG-direction infrastructure module `hysterpy.llg_grain` validated against the Stoner–Wohlfarth astroid in Supplementary Figure S13. Reproducibility: `numpy` 2.x, `scipy` 1.17, `matplotlib` 3.10, `numba` 0.62, `optuna` 4.8. The Fit seeds (`rng_seed=2025`) and Optuna study configurations for all results in this paper are documented in the corresponding fitting scripts under `scripts/` and `examples/` of the same archive.

References

1. Brown, W. F. Thermal fluctuations of a single-domain particle. *Phys. Rev.* **130**, 1677–1686, https://doi.org/10.1103/PhysRev.130.1677 (1963).
2. Coffey, W. T., Kalmykov, Y. P. & Waldron, J. T. *The Langevin Equation: With Applications to Stochastic Problems in Physics, Chemistry and Electrical Engineering* (World Scientific, 2004), 2nd edn.
3. Debye, P. *Polar Molecules* (Chemical Catalog Company, New York, 1929).
4. Baghel, A. P. S., Gupta, A., Chwastek, K. & Kulkarni, S. V. Comprehensive modelling of dynamic hysteresis loops in the rolling and transverse directions for transformer laminations. *Phys. B: Condens. Matter* **462**, 86–92, https://doi.org/10.1016/j.physb.2015.01.026 (2015).
5. Jiles, D. C. & Atherton, D. L. Theory of ferromagnetic hysteresis. *J. Magn. Magn. Mater.* **61**, 48–60, https://doi.org/10.1016/0304-8853(86)90066-1 (1986).
6. Baghel, A. P. S. & Kulkarni, S. V. Hysteresis modeling of the grain-oriented laminations with inclusion of crystalline and textured structure in a modified Jiles–Atherton model. *J. Appl. Phys.* **113**, 043908, https://doi.org/10.1063/1.4788806 (2013).
7. Chang, J. S. & Cooper, G. A practical difference scheme for Fokker–Planck equations. *J. Comput. Phys.* **6**, 1–16, https://doi.org/10.1016/0021-9991(70)90001-X (1970).
8. Buet, C. & Le Thanh, K. C. Generalized Chang-Cooper method for the discretization of Fokker-Planck equations. *Numer. Math.* **116**, 633–669, https://doi.org/10.1007/s00211-010-0317-4 (2010).
9. Chwastek, K. Modelling of dynamic hysteresis loops using the Jiles-Atherton approach. *Math. Comput. Model. Dyn. Syst.* **15**, 95–105, https://doi.org/10.1080/13873950802432016 (2009).
10. D'Aloia, A. G., Di Francesco, A. & De Santis, V. A novel computational method to identify/analyze hysteresis loops of hard magnetic materials. *Magnetochemistry* **7**, https://doi.org/10.3390/magnetochemistry7010010 (2021).
11. Mayergoyz, I. D. *Mathematical Models of Hysteresis and Their Applications* (Elsevier, 2003), 2nd edn.
12. Krasnosel'skiĭ, M. A. & Pokrovskiĭ, A. V. *Systems with Hysteresis* (Springer-Verlag, 1989).
13. Li, Y. & Luo, Z. A comparative study of J–A and Preisach improved models for core loss calculation under DC bias. *Sci. Reports* **14**, 9409, https://doi.org/10.1038/s41598-024-55155-w (2024).
14. Ramesh, A., Jiles, D. C. & Bi, Y. Generalization of hysteresis modeling to anisotropic materials. *J. Appl. Phys.* **81**, 5585–5587, https://doi.org/10.1063/1.364843 (1997).
15. Cullity, B. D. & Graham, C. D. *Introduction to Magnetic Materials* (Wiley-IEEE Press, 2008), 2nd edn.
16. Daniel, L., Hubert, O., Buiron, N. & Billardon, R. Reversible magneto-elastic behavior: A multiscale approach. *J. Mech. Phys. Solids* **56**, 1018–1042, https://doi.org/10.1016/j.jmps.2007.06.003 (2008).
17. Hubert, A. & Schäfer, R. *Magnetic Domains: The Analysis of Magnetic Microstructures* (Springer, 2008), 2nd edn.
18. Bendra, M. *Numerical Analysis and Innovative Simulation Techniques for Designing Advanced MRAM*. Ph.D. thesis, TU Wien https://doi.org/10.34726/hss.2026.118823 (2026).
19. Zirka, S. E. *et al.* Generalization of the classical method for calculating dynamic hysteresis loops in grain-oriented electrical steels. *IEEE Transactions on Magn.* **44**, 2113–2126, https://doi.org/10.1109/TMAG.2008.2000662 (2008).
20. Kestens, L. & Jacobs, S. Texture control during the manufacturing of nonoriented electrical steels. *Texture, Stress. Microstruct.* **2008**, Article ID 173083, https://doi.org/10.1155/2008/173083 (2008).
21. Xia, Z., Kang, Y. & Wang, Q. Developments in the production of grain-oriented electrical steel. *J. Magn. Magn. Mater.* **320**, 3229–3233, https://doi.org/10.1016/j.jmmm.2008.07.003 (2008).
22. Moses, A. J. Electrical steels: past, present and future developments. *IEEE Proc. A* **137**, 233–245, https://doi.org/10.1049/ip-a-2.1990.0034 (1990).
23. Zirka, S. E., Moroz, Y. I., Marketos, P. & Moses, A. J. Dynamic hysteresis modelling. *Phys. B* **343**, 90–95, https://doi.org/10.1016/j.physb.2003.08.036 (2004).
24. Ilmenauer Mechatronik GmbH. Mess- und Prüftechnik: MagHyst® modular (2023).
25. Virtanen, P., Gommers, R., Oliphant, T. E. *et al.* SciPy 1.0: Fundamental Algorithms for Scientific Computing in Python, https://doi.org/10.1038/s41592-019-0686-2 (2020).

26. Brest, J., Greiner, S., Bošković, B., Mernik, M. & Žumer, V. Self-adapting control parameters in differential evolution: A comparative study on numerical benchmark problems. *IEEE Transactions on Evol. Comput.* **10**, 646–657, https://doi.org/10.1109/TEVC.2006.872133 (2006).

27. Tanabe, R. & Fukunaga, A. S. Improving the search performance of SHADE using linear population size reduction. In *2014 IEEE Congress on Evolutionary Computation (CEC)*, 1658–1665, https://doi.org/10.1109/CEC.2014.6900380 (2014).

28. Storn, R. & Price, K. Differential Evolution: A simple and efficient heuristic for global optimization over continuous spaces. *J. Glob. Optim.* **11**, 341–359, https://doi.org/10.1023/A:1008202821328 (1997).

29. Brun, R., Reichert, P. & Künsch, H. R. Practical identifiability analysis of large environmental simulation models. *Water Resour. Res.* **37**, 1015–1030, https://doi.org/10.1029/2000WR900350 (2001).

30. Fiorillo, F., Dupre, L. R., Appino, C. & Rietto, A. M. Comprehensive model of magnetization curves, hysteresis loops, and losses in any direction in grain-oriented fe–si. *IEEE Transactions on Magn.* **38**, 1467–1476, https://doi.org/10.1109/20.999119 (2002).

31. Pry, R. H. & Bean, C. P. Calculation of the energy loss in magnetic sheet materials using a domain model. *J. Appl. Phys.* **29**, 532–533, https://doi.org/10.1063/1.1723212 (1958).

32. Shilling, J. W., Morris, W. G., Osborn, M. L. & Rao, P. Orientation dependence of domain wall spacing and losses in 3-percent si-fe single crystals. *IEEE Transactions on Magn.* **14**, 104–109, https://doi.org/10.1109/TMAG.1978.1059682 (1978).

33. Daalderop, G. H. O., Kelly, P. J. & Schuurmans, M. F. H. First-principles calculation of the magnetocrystalline anisotropy energy of iron, cobalt, and nickel. *Phys. Rev. B* **41**, 11919–11937, https://doi.org/10.1103/PhysRevB.41.11919 (1990).

34. Trygg, J., Johansson, B., Eriksson, O. & Wills, J. M. Total energy calculation of the magnetocrystalline anisotropy energy in the ferromagnetic 3d metals. *Phys. Rev. Lett.* **75**, 2871–2874, https://doi.org/10.1103/PhysRevLett.75.2871 (1995).

35. Sablik, M. J. & Jiles, D. C. Coupled magnetoelastic theory of magnetic and magnetostrictive hysteresis. *IEEE Transactions on Magn.* **29**, 2113–2123, https://doi.org/10.1109/20.221036 (1993).

36. Jiles, D. C. Frequency dependence of hysteresis curves in conducting magnetic materials. *J. Appl. Phys.* **76**, 5849–5855, https://doi.org/10.1063/1.358399 (1994).

37. Nourdine, A., Kedous-Lebouc, A., Meunier, G. & Chevalier, T. A new hysteresis model based on thermodynamics for magnetization curves. *IEEE Transactions on Magn.* **36**, 1230–1233, https://doi.org/10.1109/20.877662 (2000).

38. Nourdine, A., Kedous-Lebouc, A., Meunier, G. & Chevalier, T. Quasi-static RD and TD hysteresis modelling using a thermodynamic description. *IEEE Transactions on Magn.* **37**, 3340–3344, https://doi.org/10.1109/20.952613 (2001).

39. Bertotti, G. General properties of power losses in soft ferromagnetic materials. *IEEE Transactions on Magn.* **24**, 621–630, https://doi.org/10.1109/20.43994 (1988).

40. Baghel, A. P. S., Sai Ram, B., Chwastek, K., Daniel, L. & Kulkarni, S. V. Hysteresis modelling of GO laminations for arbitrary in-plane directions taking into account the dynamics of orthogonal domain walls. *J. Magn. Magn. Mater.* **418**, 14–20, https://doi.org/10.1016/j.jmmm.2016.02.007 (2016).

41. Bergstra, J., Bardenet, R., Bengio, Y. & Kégl, B. Algorithms for hyper-parameter optimization. In *Advances in Neural Information Processing Systems 24*, 2546–2554 (2011).

42. HEFMAG Consortium, INRiM, PTB, NPL & CMI. Wideband hysteresis and complex-permeability dataset for grain-oriented and non-oriented FE-SI, amorphous and nanocrystalline ribbons (empir 19eng06), https://doi.org/10.5281/zenodo.5910892 (2022).

43. Silva, V. *et al.* Nog FE-SI hysteresis loops under uniaxial stress, three directions (rd/td/dd), three frequencies, https://doi.org/10.17632/hgzgpcvjxk.1 (2025).

44. Silveyra, J. M. & Conde Garrido, J. M. mag-analyst: open-source double langevin–weiss hysteresis fitting tool (2022).

45. Conde Garrido, J. M., Ugarte Valdivielso, J., Aizpurua, J. I., Barrenetxea Iñarra, M. & Silveyra, J. M. Blind efficient method for optimizing Jiles–Atherton model parameters. *IEEE Transactions on Magn.* https://doi.org/10.1109/TMAG.2025.3632479 (2025).

46. Dias, M. B. S. *et al.* Magnetic and microstructural properties of uncoated, shear-cut electrical steel under localized compressive stress and heat treatment, https://doi.org/10.17632/fb6jp8t374.2 (2020).

47. Bozorth, R. M. *Ferromagnetism* (Wiley-IEEE Press, 1993).

Acknowledgements

The Johannes Kepler University Library Open Access Publishing Fund supported this work.

Funding

This work was performed at the JKU Hoerbiger Research Institute for Smart Actuators, Johannes Kepler University Linz, which is funded by HOERBIGER.

Author contributions statement

Conceptualization, methodology, software, validation, formal analysis, investigation, data curation, visualization, and writing (original draft as well as review and editing): M.B. Supervision and writing (review and editing): F.P. Both authors have read and approved the final manuscript.

Additional information

Competing interests: The authors declare no competing interests.

Supplementary Files

This is a list of supplementary files associated with this preprint. Click to download.

- SupplementaryInformationforAunifiedratedependentanisotropichysteresismodelforgrainorientednonorientedanddirectionalelectrical.zip